

Resolution and aberration correction in liquid cell transmission electron microscopy

Niels de Jonge^{1,2}, Lothar Houben^{3,4}, Rafal E. Dunin-Borkowski³ and Frances M. Ross^{5,6*}

Abstract | Liquid cell electron microscopy possesses a combination of spatial and temporal resolution that provides a unique view of static structures and dynamic processes in liquids. Optimizing the resolution in liquids requires consideration of both the microscope performance and the properties of the sample. In this Review, we survey the competing factors that determine spatial and temporal resolution for transmission electron microscopy and scanning transmission electron microscopy of liquids. We discuss the effects of sample thickness, stability and dose sensitivity on spatial and temporal resolution. We show that for some liquid samples, spatial resolution can be improved by spherical and chromatic aberration correction. However, other benefits offered by aberration correction may be even more useful for liquid samples. We consider the greater image interpretability offered by spherical aberration correction and the improved dose efficiency for thicker samples offered by chromatic aberration correction. Finally, we discuss the importance of detector and sample parameters for higher resolution in future experiments.

The driving force behind the development of liquid cell, or liquid phase, electron microscopy has been its high spatial resolution compared with that of other microscopies that work in liquid, such as light microscopy^{1–5}. Good temporal resolution is a second key benefit, again compared with other microscopies that work in liquid, such as scanning probe microscopy. This combination of spatial and temporal resolution places electron microscopy in a unique niche for imaging both static structures and dynamic processes in liquids. To optimize experimental design and obtain the most useful information, it is important to understand the factors that limit the resolution of liquid cell electron microscopy⁶. The intrinsic capabilities of the microscope (for example, its stability and whether lens aberrations are corrected) have a role in determining spatial and temporal resolution, but so do the thickness, stability and dose sensitivity of the sample. The microscope performs at its full resolution for conventional samples that are thin, stable and solid⁷, but liquid samples have particular challenges. Liquid samples may be unusually thick⁸, are often beam-sensitive, similar to samples used in cryo-electron microscopy, and may also have a dynamic nature, such as liquids in which suspended particles undergo Brownian motion⁹. These three properties — thickness, sensitivity and dynamics — determine which factors limit the

spatial and temporal resolution and whether benefits are expected from aberration correction in a liquid imaging experiment.

In this Review, we discuss resolution and aberration correction for the most common types of liquid samples. The most frequently used liquid enclosure is a microfabricated liquid cell consisting of silicon nitride membranes¹⁰ or windows, ~50 nm thick, enclosing a water layer tens of nanometres to a few micrometres in thickness. The sample under observation comprises the enclosed liquid, the windows and nanoscale objects that can be mobile in the liquid or attached to the interior surfaces of the windows. A second type of liquid enclosure consists of graphene sheets^{5,11} that encapsulate a small liquid volume of thickness typically <100 nm. Unlike microfabricated liquid cells, which are relatively thick, the graphene liquid enclosure may be no thicker than the solid samples conventionally used in electron microscopy. Good spatial and temporal resolution has been demonstrated for both microfabricated and graphene liquid cells^{4,5,8,12–16}.

Other liquid geometries are also possible. For example, a thin water layer can be maintained and imaged in an environment of saturated water vapour by controlling the pressure and temperature to establish equilibrium between the water and vapour^{17,18}, and

¹INM — Leibniz Institute for New Materials, Saarbrücken, Germany.

²Department of Physics, Saarland University, Saarbrücken, Germany.

³Ernst Ruska-Centre for Microscopy and Spectroscopy with Electrons and Peter Grünberg Institute, Forschungszentrum Jülich, Jülich, Germany.

⁴Department of Chemical Research Support, Weizmann Institute of Science, Rehovot, Israel.

⁵IBM T. J. Watson Research Center, Yorktown Heights, NY, USA.

⁶Department of Materials Science and Engineering, Massachusetts Institute of Technology, Cambridge, MA, USA.

*e-mail: fmross@mit.edu

<https://doi.org/10.1038/s41578-018-0071-2>

ionic liquids with low vapour pressure can be imaged without the need for any enclosure or environmental control¹⁹. Aspects of the discussion below, in particular beam damage considerations, are relevant to such ‘open cell’ experiments.

As we show below, sensitivity to the electron beam is very often the factor limiting spatial and temporal resolution in electron microscopy of liquids. We therefore start by discussing beam effects in water and practical limitations on dose in transmission electron microscopy (TEM) and scanning TEM (STEM). We then consider the limits to spatial resolution in TEM and show that although resolution in thin liquid layers may be limited by electron optics, resolution is more commonly limited by dose sensitivity. We also discuss competing factors in experimental design, such as the trade-off between resolution and liquid thickness. We next describe the resolution enhancement and other benefits expected for TEM imaging of liquids from spherical aberration (C_s) and chromatic aberration (C_c) correction. Aberration correction has not been widely applied to liquid imaging; therefore, parts of the discussion are hypothetical. However, C_s correction produces images that are easier to interpret and improves the resolution in cases in which resolution is not otherwise limited (for example, by dose considerations). C_s correction should prove especially useful in experiments that use strong illumination conditions, such as those probing nanoparticle growth. C_c correction should be particularly useful for energy-filtered TEM (EFTEM) imaging and for dose-efficient imaging of thicker samples. Moreover, C_c correction can, in principle, also benefit experiments involving holography and phase plates. We also assess the resolution in STEM of liquid samples, showing that the signal-to-noise ratio (SNR) is the critical limiting factor under most conditions. Finally, we discuss the temporal resolution for both TEM and STEM. Resolution in scanning electron microscopy (SEM) of liquids is discussed elsewhere²⁰.

The acceptable dose for liquid samples

For any sample, a critical dose can be defined as the threshold of absorbed energy (per mass) at which structural changes start to occur. There is no single value for the critical dose: it ranges over orders of magnitude depending on the sample, type of imaging and dose rate. Note that in the electron microscopy literature, the term electron dose is often used to indicate the number of electrons that have irradiated a given area (with units such as $e^- \text{Å}^{-2}$), but this quantity is more correctly referred to as the electron density, D . Similarly, the electron dose rate, often used in the literature, is perhaps better termed the electron flux (with units $e^- \text{Å}^{-2} \text{s}^{-1}$). Experimentally, it is the critical electron density, D_c , at which damage becomes visible, rather than the dose, that is measured. The accelerating voltage, other microscope settings and, of course, the materials present in the sample and its surroundings determine the amount of radiation damage. Some damage is inevitable regardless of the parameters chosen. For example, the main damage mechanisms, radiolysis and knock-on interactions, have opposite dependences on accelerating voltage²¹;

the optimal voltage for damage may differ between the material in the sample and in the enclosing windows.

The number of incident electrons that the sample can tolerate without damage is a key factor in determining image resolution. Calculating D_c is difficult because of the variety and complexity of interactions between the beam, liquid and window materials²². The high thermal conductivity of water renders beam-induced temperature rises negligible under typical conditions⁹. However, radiolysis of water produces chemically active species that can diffuse and interact within the liquid, even outside the irradiated area²³. Furthermore, the window materials may be damaged through charging and material loss²⁴. High-dose analytical measurements or time series that require multiple images will exacerbate these effects.

As it is not possible to fully eliminate beam damage or easily calculate damage thresholds, it is necessary to establish the limits experimentally. A good starting point is the cryo-electron microscopy literature. However, cryo-electron microscopy reports provide guidance rather than exact values owing to the differences between imaging in water and ice. Most importantly, liquid cell electron microscopy experiments are carried out at a higher temperature than cryo-electron microscopy experiments, usually at the ambient microscope temperature of 25–30 °C; the thermal conductivity of a liquid sample is greater than that of a typical cryo-electron microscopy sample; differences are expected in both formation rate and diffusion of radiolysis species; and liquid flow provides new opportunities for removing radiolysis species and refreshing the sample environment⁴.

For cryo-electron microscopy measurements, there is approximately an order of magnitude variation in the value at which damage to biomaterials in ice has been detected in images. A D_c of $\sim 10 e^- \text{Å}^{-2}$ was established for sub-nanometre imaging of protein structures using single-particle tomography^{25,26}, whereas a less stringent D_c of $\sim 10^2 e^- \text{Å}^{-2}$ was established for imaging cellular ultrastructure²⁷. These values differ because the information provided by each experiment is different. Single-particle tomography provides a resolution of up to 2–3 Å. In this case, only a low dose can be tolerated because damage appears at the sub-nanometre scale when bonds between atoms are broken and atomic-level structural features start to disintegrate. By contrast, imaging cellular ultrastructure provides information at a resolution of around only a few nanometres, and thus some degree of structural damage at smaller length scales can be tolerated.

Given these critical limits for cryo-electron microscopy, the key questions are whether and how much the situation differs for imaging in water and whether the same general principle applies — that the higher the desired resolution, the more stringent D_c becomes. Early data suggested a D_c of $1 e^- \text{Å}^{-2}$ as the limit for sub-nanometre structural preservation of biomolecules in a thin water layer²⁸. This D_c is lower than the cryo-electron microscopy D_c range given above. However, values as high as $\sim 35 e^- \text{Å}^{-2}$ for imaging with 2.6 nm resolution have also been reported²⁹, which is higher than

the values in cryo-electron microscopy. Dynamic processes involving DNA have been observed³⁰ at electron fluxes of $110 \text{ e}^- \text{ \AA}^{-2} \text{ s}^{-1}$. Allowing for chemical fixation, an even higher D_c of $10^3 \text{ e}^- \text{ \AA}^{-2}$ is possible before damage becomes visible for whole mammalian cells in liquid³¹. This suggests that D_c is higher for samples involving liquid water than those involving ice. The difference between the D_c for damage in water and damage in ice may relate to the easier diffusion of reactive species away from the irradiated region in a liquid environment. It is also possible³⁰ that charge pairs created by irradiation may recombine more easily through diffusion in liquid water than in ice, as long as the total charge density remains sufficiently small. An important objective for future experiments will be to establish the experimental conditions for which TEM in water improves D_c compared with that in ice.

For biological materials, acceptable D_c values will also be different when aiming to probe cellular functions. Cellular functions may be disrupted, and ultimately, cells may die by radiation even if there are no physical changes in structure. Experiments show that lethal D_c values for cells are exceeded by orders of magnitude when even a single image is obtained^{32–34}. Instead, dynamic processes in cells can be examined using correlative fluorescence microscopy, with electron microscopy used to record single images of selected regions at a specific time^{32,34,35}.

The electron flux also has an important role in the radiation damage process in biological samples³⁶. Because damage depends on both the incoming irradiation and the processes that distribute the absorbed energy, specifically the diffusion of charge, heat and chemically active species, we expect beam effects on the sample to depend on the electron flux. For example, liquid cell measurements of the growth of lysozyme protein crystals³⁷ showed that a flux of $3 \text{ e}^- \text{ \AA}^{-2} \text{ s}^{-1}$ negligibly affects growth, whereas a flux ten times higher dissolves crystals.

The D_c and electron flux considerations discussed above for biomaterials do not necessarily constrain imaging of other types of liquid samples. For example, consider a commonly imaged sample consisting of high-atomic-number (Z) metal nanoparticles in water. Conventional imaging of thin metal foils at atomic resolution typically involves a D of up to $10^4 \text{ e}^- \text{ \AA}^{-2}$. Thus, it is not surprising if the D_c for metal nanoparticles in water is higher than that for biological materials in water. Metal and other nanoparticles have indeed been imaged in liquid with atomic resolution^{12–15}. However, even these samples can show sensitivity to the beam. For PbO_2 nanoparticles, sub-nanometre information disappears¹⁶ after exposure to a D of $10^2 \text{ e}^- \text{ \AA}^{-2}$, suggesting a D_c that is only slightly higher than that for biological material.

To evaluate the dose sensitivity of such nanoparticle-in-water samples, it is necessary to consider the invisible effects of the beam on the chemistry of the surrounding water. To this end, radiolysis modelling³⁸ has shown that electron flux is the key parameter and is generally more important than electron density in determining beam-induced chemical changes. Radiolysis species are created even under the lowest electron flux used for imaging, with the resulting chemical changes reaching,

in milliseconds, a steady state that depends on the flux. As an example, the pH of water is expected³⁸ to change from 7 to 5 upon irradiation at $20 \text{ e}^- \text{ \AA}^{-2} \text{ s}^{-1}$. Changes in pH alter electrochemical reactions and nanoparticle stability³⁹. Other products of radiolysis, such as hydrated (solvated) electrons, drive reactions such as the reduction of dissolved ionic species to initiate the growth of metal nanoparticles^{12,13}. In agreement with radiolysis modelling, experiments show that electron flux, rather than electron density, controls the kinetics observed during, for example, nanoparticle growth⁴⁰. In experiments in which the electron beam is used deliberately to initiate nanoparticle growth or other types of materials reactions, typical imaging involves strong illumination of $\sim 10^3 \text{ e}^- \text{ \AA}^{-2} \text{ s}^{-1}$ (REF.⁴¹). As we discuss below, the high number of electrons per image accounts for the excellent spatial resolution often obtained in images of these materials processes.

Given the importance of dose in imaging liquid samples, it is essential to further increase our understanding of beam effects, to optimize the sample in response to dose considerations and to use every electron optimally. Parallel application of cryo-electron microscopy and liquid cell microscopy will help to clarify the effect of electron density and flux. The thickness of the liquid and windows should be chosen to maximize the signal-to-background ratio⁶. In STEM, the probe size should match the desired resolution; in TEM, illumination outside the recorded area (for example, the use of a large spread beam) should be avoided. Electron microscopy of liquids benefits from modern detectors with high quantum efficiency⁴². Cameras offering high-speed acquisition can be used for dose fractionation, in which a series of sub-frames, instead of a single exposure, is recorded and then aligned to improve contrast in the presence of sample motion⁴³. This strategy will also enable the onset of damage to be detected so that only data obtained before this time are used. Low-dose methods, used for decades in structural biology, will likely be beneficial for some types of liquid samples. Single-particle tomography²⁵ averages thousands of identical particles imaged at low dose. Intelligent acquisition schemes can be used to concentrate the dose at the most useful regions of the sample and minimize unnecessary dose. In particular, sparse imaging and adaptive scanning techniques can reduce the dose by more than an order of magnitude⁴⁴ by directing the dose to locations of the sample with the highest information content. Analogously, for time-dependent phenomena, it has been proposed that the temporal distribution of the dose be adjusted to favour the times at which the sample is changing the most rapidly or that temporal compressive sensing techniques be used to provide higher image acquisition rates without increasing the dose⁴⁵. Whatever strategy is used, it is important to measure and report the electron density history and electron flux.

Spatial resolution in liquid cell TEM

Spatial resolution in TEM of liquids is determined by several factors, which depend on the thickness and beam sensitivity of the sample. We first discuss thin samples, such as liquid pockets encapsulated in graphene, for which C_s and beam sensitivity determine

resolution. However, liquid samples are often thicker than the very thin samples typically used in TEM when the highest resolution is obtained. Microfabricated liquid cell samples may require a thick liquid layer to support the material or process under study or to achieve liquid flow or electrical connections, and the windows must also be thick in order to withstand the vacuum environment without excessive deflection. Even graphene liquid cells are thin only around the edges of the encapsulated droplets. In the thick sample limit, we consider C_c and beam sensitivity effects. We next discuss the depth of an object within the liquid layer. Finally, we describe some practical aspects of experimental design that affect resolution.

Thin samples with C_s -limited resolution. In conventional high-voltage TEM of thin samples, the spatial resolution is limited by lens aberrations, particularly C_s in the objective lens. Typical uncorrected transmission electron microscopes show resolutions of around 0.17 nm (at 400 keV) or 0.24 nm (at 200 keV). We would expect to achieve this resolution for a thin liquid sample in the absence of limits due to dose sensitivity and neglecting the effects of motion. Imaging at this resolution has indeed been shown in both silicon-nitride-encapsulated and graphene-encapsulated liquids^{12–15}.

Dose-limited resolution in TEM. The dose sensitivity of liquid samples creates a resolution limit that generally dominates over the effects of lens aberrations. To evaluate the resolution in liquid, assuming that the electron optics are not limiting, we consider an image acquired at low D (so that $D < D_c$). Owing to statistical noise, an object can be detected reliably in the image only if the corresponding pixels have a signal level above the background counts with sufficient magnitude that the SNR exceeds a value of 3–5 (known as the Rose criterion⁴⁶). When imaging an object in liquid, background scattering in the liquid is the origin of the observed statistical fluctuations in the image, and detector noise is typically negligible. The SNR in the image is given by^{21,47}:

$$\begin{aligned} \text{SNR} &= \text{DQE}^{1/2} |\Delta N| / \langle N \rangle^{1/2} \\ &= \text{DQE}^{1/2} C \langle N \rangle^{1/2} \end{aligned} \quad (1)$$

Here, DQE is the detector quantum efficiency, and the background pixels scatter $\langle N \rangle$ electrons on average into the detector, resulting in a noise level of $\langle N \rangle^{1/2}$, while the object scatters $N + \Delta N$ electrons for a signal of $|\Delta N|$. The SNR is thus a function of the contrast $C = |\Delta N| / \langle N \rangle$, which depends on the imaging mode and the materials that make up the sample.

A TEM camera collects $\langle N \rangle = Ds^2$ electrons from a specimen area comprising a pixel of size s when exposed to electron density D . Substituting for $\langle N \rangle$ in equation 1 and assuming $\text{SNR} = 3$ reveals that an object of contrast C is detectable only if both object size and s exceed²¹:

$$s = 3\text{DQE}^{-1/2} C^{-1} D^{-1/2} \quad (2)$$

This minimum s is approximately equal to the dose-limited resolution⁴⁷, d_D , if C is regarded as a constant. As an example, consider a 5 nm carbon object representing a biological sample with $C = 5\%$. If $\text{DQE} = 0.2$ (as in a standard TEM camera) and $D_c = 100 \text{ e}^- \text{ \AA}^{-2}$, the object can be imaged with $d_D \approx 4 \text{ nm}$, consistent with results for cryo-TEM of cells²⁷. More generally, equation 2 can be used to estimate the dose range for which a certain resolution is possible (FIG. 1). The key message is that the dose acceptable to the sample often controls the resolution. However, it is important to note that equation 2 neglects the variation of C with object size. Nanoparticles, for example, generally have approximately the same height and width, so that wider objects would also show higher contrast. If a specific relationship like this exists between contrast and sample geometry or composition, the general guidance that equation 2 provides can be made more precise, as we discuss below.

Thin samples with dose-limited phase contrast. Phase-contrast equations apply when the sample is thinner than about half the total mean free elastic scattering path length, which is $\sim 160 \text{ nm}$ in water⁶. The phase-contrast equations lose their validity for thicker samples because the coherence of the electron wave is lost owing to scattering, and bright-field imaging equations then apply.

Consider the specific case of an object, such as a protein in water, for which contrast arises because the electron wave passing through the object experiences a slightly different phase change compared with the electron wave travelling past the object. As a consequence, C is not a constant but a function of the scattering properties and dimensions of the object⁴⁸:

$$C = \left\{ N_o f_{el}^o(0) - N_w f_{el}^w(0) \right\} \frac{2}{3} t_o \lambda = C^* \frac{2}{3} t_o \quad (3)$$

Here, t_o is the object thickness; λ is the electron wavelength; N_o and N_w are the number of atoms per unit volume for the object and water (or other liquid), respectively; and $f_{el}(0)$ is the zero-angle elastic scattering factor for either the object, f^o , or water, f^w (see Supplementary information). C as defined here can be thought of as the intrinsic contrast per unit length. Liquid below and above the object does not contribute to C but does reduce the coherence of the electron beam for thicker layers, which is an effect not included in equation 3. For an object of $t_o = 5 \text{ nm}$, equation 3 gives $C = 0.05$ and 0.1 for carbon and gold, respectively. Note that the Bragg contrast of nanocrystals can be much higher than equation 3 implies, owing to the effect of multiple coherent elastic scattering. Bragg contrast can therefore enhance the SNR and resolution when compared with the independent atom model considered here.

The SNR-limited resolution of phase-contrast TEM, d_{phase} , equals the minimum object size that can be detected with sufficient SNR and is calculated assuming that t_o equals the object size in all dimensions so that $d_{\text{phase}} = t_o$. If the TEM image pixel size is adjusted

(by changing the magnification) for optimal sampling (determined using the Nyquist criterion, which stipulates that s is half the inverse of the detected spatial frequency or resolution, $s = d_{\text{phase}}/2$) and it is assumed that the object under observation has approximately the same size in all dimensions, equations 2 and 3 can be combined to result in an expression for the SNR-limited resolution for phase-contrast TEM⁶:

$$d_{\text{phase}} = 3/2C^{*-1/2}\text{DQE}^{-1/4}D^{-1/4} \quad (4)$$

Equation 4 provides an estimate of the achievable spatial resolution for imaging approximately spherical objects in water. For elongated objects, the shorter dimension is considered. Note that the equation neglects variations in the contrast transfer

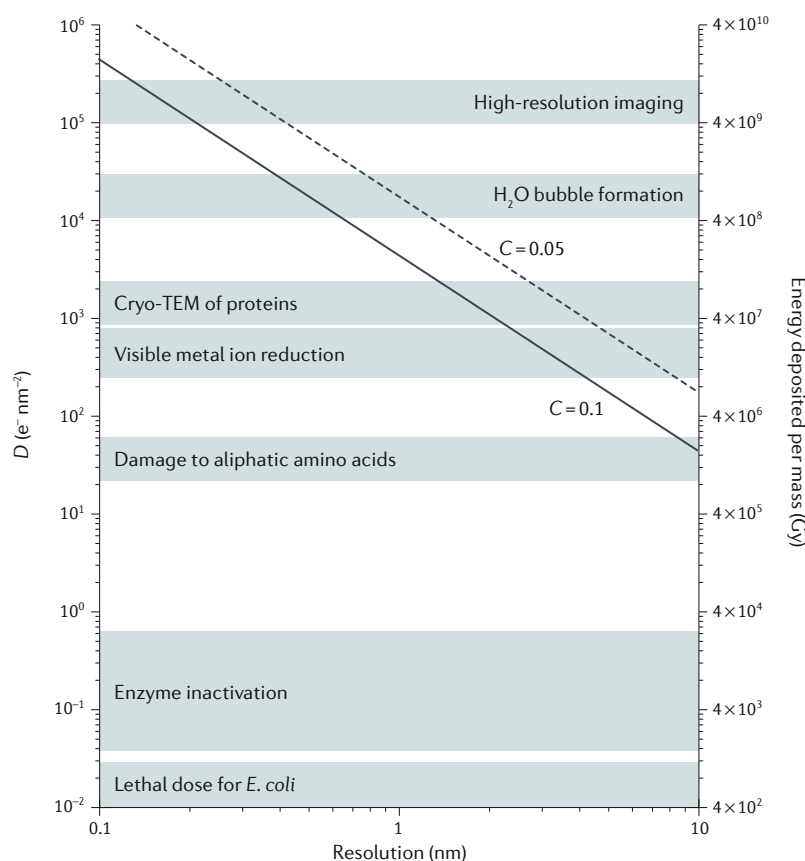


Fig. 1 | Electron density required to reach a desired spatial resolution at 200 keV for typical materials. Results of equation 2 for transmission electron microscopy (TEM) with a detector quantum efficiency of 0.2 and typical object properties and dimensions. Contrast C of 0.05 (dashed line) or 0.1 (solid line) is used to approximate biological samples and gold nanoparticles, respectively. The y axis on the right-hand side gives the dose for both contrast values in Grays (Gy; that is, the energy deposited per unit of mass, J kg^{-1}), assuming $1 \text{ e}^- \text{ nm}^{-2} \approx 4 \times 10^4 \text{ Gy}$, a typical value for water at 200 keV. Acceptable electron density (D) ranges and some beam-induced phenomena are shown as horizontal bands. The lethal D for *Escherichia coli* is $\sim 0.01 \text{ e}^- \text{ nm}^{-2}$ (REF.²¹), and the D for enzyme inactivation is $\sim 1 \text{ e}^- \text{ nm}^{-2}$. The D for visible metal ion reduction, based on data from REFS^{36,40,123} for the reduction of Ag^+ and Au^{3+} ions to form metal nanoparticles, is several hundred $\text{e}^- \text{ nm}^{-2}$ and above. This range is broad and can be higher in other experiments because of the importance of dose rate and solution chemistry. Adapted with permission from REF.¹²⁴, Cambridge University Press.

function. An important implication of equation 4 is that the resolution for imaging nanoparticles scales as $d_{\text{phase}} \sim D^{-1/4}$ (REF.⁶), a much stronger dependence than would be expected if C were constant. This means that improving the resolution requires a much higher D but also shows that there is an advantage to choosing a slightly lower resolution when imaging beam-sensitive materials.

Thick samples with C_c -limited resolution. Inelastic scattering in thick liquid samples, lens instabilities and the intrinsic energy spread of the source all contribute to a spread in energy of the electrons that form the image. This energy spread reduces the resolution because of C_c . In cases in which C_c dominates, the image resolution is given by²¹:

$$d_c = 0.5c_c\alpha\left(\frac{\Delta E}{E}\right)\frac{1+E/E_0}{1+E/2E_0} \quad (5)$$

where d_c is the chromatic blur, α is the objective aperture semi-angle, c_c is the chromatic aberration coefficient, ΔE is the spread in energy of a beam of energy E and E_0 is the rest energy ($m_0c^2 = 511 \text{ keV}$, where m_0 is the rest mass of the electron and c is the speed of light). Liquid samples are generally thick enough to produce a high probability of inelastic scattering events that broaden the range of transmitted electron energies compared with the spread at the source. ΔE increases with the sample thickness until C_c dominates the resolution, and thus the resolution can be calculated by relating ΔE to the inelastic scattering properties of the liquid. The full width at half maximum of the transmitted energy spread follows from calculations of the inelastic electron scattering cross section and is given by²¹:

$$\Delta E = \frac{N_A e^4 Z \rho t}{2\pi \epsilon_0^2 W m_0 v^2} \quad (6)$$

where N_A is Avogadro's number, e is the elementary charge, W is the atomic weight, Z is the atomic number, ρ is the density of the liquid layer, t is the thickness of the liquid layer, ϵ_0 is the permittivity of space and v is the velocity of the electrons. For water, where $Z = 4.7$ (REFS^{4,49}), and in the non-relativistic case, these equations can be combined into an estimate for the resolution³:

$$d_{c,\text{TEM}} = 6 \times 10^{12} \alpha c_c t / E^2 \quad (7)$$

with E in eV. Neglecting the windows and using the typical parameters $\alpha = 10 \text{ mrad}$, $c_c = 2 \text{ mm}$, $E = 200 \text{ keV}$ and $t = 1 \text{ }\mu\text{m}$, we obtain for water $d_{c,\text{TEM}} = 3 \text{ nm}$. This value applies for objects at the beam exit side of the liquid layer and imaged at high D , as discussed below. However, note that the value increases by a factor of two if relativistic effects are considered. The resolution observed in many liquid cell experiments is consistent with predictions based on equation 7, which emphasizes the importance of chromatic blur for TEM of liquids³.

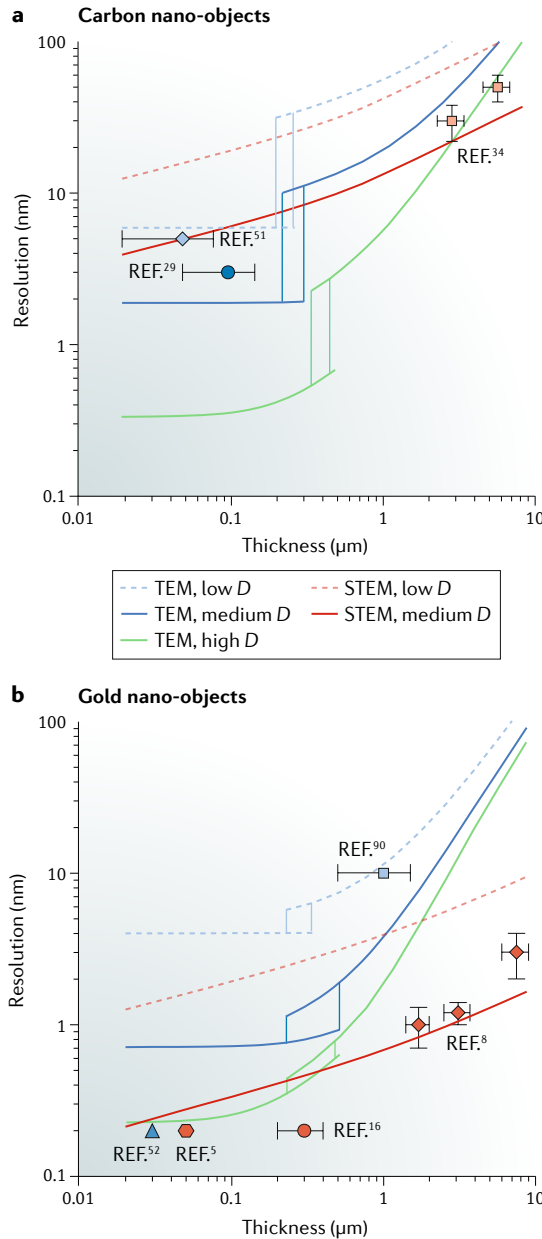


Fig. 2 | Theoretical maximum image resolution versus thickness of water. Calculated transmission electron microscopy (TEM) and scanning TEM (STEM) resolutions for spherical nano-objects composed of carbon (panel a) and gold (panel b) in water. The resolutions are calculated for different electron densities, D . For TEM, phase-contrast and bright-field contrast equations apply to thin and thick water layers, respectively. The exact transition thickness is unknown, as indicated by the vertical lines. The resolution was calculated assuming no limitation by diffraction or lens aberrations, a beam energy of 200 keV, a 5 mrad objective aperture for bright-field contrast, a TEM camera detector quantum efficiency of 20%, an optimized STEM annular dark-field detector opening angle, the objects located at the electron entrance (for STEM) or exit (for TEM) surfaces and a negligible window thickness. High $D = 10^5 \text{ e}^- \text{ \AA}^{-2}$, low $D = 1 \text{ e}^- \text{ \AA}^{-2}$ and medium $D = 10^2 \text{ e}^- \text{ \AA}^{-2}$ and $10^3 \text{ e}^- \text{ \AA}^{-2}$ for carbon and gold, respectively, reflecting typical experimental values. Experimental data points^{5,8,16,29,34,51,52,90} acquired at approximately corresponding D are included for comparison.

Thick samples with dose-limited bright-field contrast.

Even with chromatic blur, the resolution for thicker samples imaged at low dose is again limited by SNR. In this case, bright-field contrast applies, and the electrons are elastically scattered out of the primary beam beyond a given α . With N_0 electrons in the primary beam, the fraction N/N_0 of electrons reaching the camera is given by^{6,21}:

$$N/N_0 = \exp\{-t/l(\alpha)\} \tag{8}$$

where $l(\alpha) = W/\sigma(\alpha)\rho N_A$. Here, $l(\alpha)$ is the mean free path for elastic scattering, which is a function of the partial elastic cross section $\sigma(\alpha)$ (see Supplementary information) and the projected charge density, $W/\rho N_A$. Inelastic scattering is neglected here as a first approximation because it occurs mostly at small scattering angles^{6,21}; for thicker samples, inelastic scattering becomes more prominent, and energy filtering would increase the contrast⁵⁰. The signal at the object is⁶:

$$N_{\text{signal}}/N_0 = \exp\{-[t_o/l_o(\alpha) + (t-t_o)/l_w(\alpha)]\} \tag{9}$$

where l_o and l_w are the mean free path lengths for the object and water (or other liquid), respectively. The signal thus depends on the object thickness, t_o . The background signal of the water is:

$$N_{\text{bkg}}/N_0 = \exp\{-t/l_w(\alpha)\}. \tag{10}$$

The SNR is then:

$$\text{SNR} = \left| N_{\text{signal}} - N_{\text{bkg}} \right| / N_{\text{bkg}}^{1/2} \tag{11}$$

The dose-limited resolution of bright-field TEM contrast, d_{bf} , is obtained by numerically solving equation 11, setting $d_{\text{bf}} = t_o$ for a spherical object and substituting⁶:

$$N_0 = D \text{ DQE } s^2 = D \text{ DQE } (d_{\text{bf}}/2)^2 \tag{12}$$

following the Nyquist criterion. Bright-field contrast is less dose-efficient than phase contrast, but for imaging spherical nano-objects, it also yields a resolution that scales as $\sim D^{-1/4}$ (REF.⁶).

Achievable resolution. The achievable TEM resolution for objects at the beam exit side of the sample is calculated by combining, through quadratic addition, the above contributions: the C_c limit, the dose-limited bright-field contrast resolution and the dose-limited phase-contrast resolution^{6,48}. The achievable resolutions are shown in FIG. 2 for several electron densities for carbon and gold nano-objects in water. For carbon nano-objects in thin water layers, phase-contrast TEM is predicted to achieve a resolution of 2 nm for $D = 10^2 \text{ e}^- \text{ \AA}^{-2}$, a typical D value used for the cryo-TEM of cellular ultrastructure²⁷, or 6 nm for $D = 1 \text{ e}^- \text{ \AA}^{-2}$. These results are consistent with experimental data^{29,51} obtained with comparable D (5 and $35 \text{ e}^- \text{ \AA}^{-2}$, respectively). In a thicker water layer, for which bright-field TEM contrast applies, the lower dose efficiency reduces the resolution.

An important question will be to determine the liquid thicknesses at which phase-contrast transitions to bright-field contrast, as well as how the transition thickness depends on D . For gold nano-objects in thin water layers, sub-nanometre resolution is expected at the high D values possible for beam-tolerant samples, whereas poorer resolution is expected for very thick ($>1\ \mu\text{m}$) liquid layers. Note, in particular, the poor resolution predicted at low dose by these calculations. A resolution several times higher (lower value in nanometres) than that calculated here has been reported for platinum nanoparticles^{5,52}. Resolutions higher than predicted in FIG. 2 may be obtainable if D is higher or if the liquid layer is thinner than reported (for example, if only a wetting layer of liquid is present). However, it is also important to note that lattice fringes can provide high contrast compared with the model used for equation 4. Equation 4 specifically involves the SNR due to a non-diffracting nanoparticle in a liquid layer⁴⁶. When nanocrystals produce high-contrast lattice fringes based on nonlinear coherent diffraction, the resolution expected at a given D is higher than the calculated resolution in FIG. 2. The same caveat applies for the calculations below.

Effect of object depth within the liquid. For a liquid layer that is several mean free path lengths in thickness, the image will differ depending on whether the object of interest (for example, a crystal growing in the liquid) is on the entrance or exit surface of the liquid cell (FIG. 3a). This so-called top–bottom effect is well known for thick samples in both TEM (FIG. 3b–f) and STEM (FIG. 3g,h). The resolution is reduced by (multiple) elastic scattering, described within a factor of two accuracy by^{6,21}:

$$x_{25-75} = 5.8 \times 10^{20} \lambda^2 \sqrt{\frac{\rho}{W}} Z(1 + E/E_0) z^{\frac{3}{2}} \quad (13)$$

Here, x_{25-75} is the rising edge width going from 25% to 75% of the maximal signal, and z is the vertical distance from the object to the beam exit point, thus measuring the total path length over which beam broadening arises.

For TEM, the highest resolution for an object in a thick ($>200\ \text{nm}$) liquid layer is achieved when the object is at the electron-beam exit side of the sample so that $z=0$ and there is no resolution loss as a result of the top–bottom effect. (The case for STEM is discussed below). The resolution in a thick sample given by equation 7 is therefore the best possible case at high D . Objects further from the exit side of the liquid layer are imaged with lower resolution³ because elastic scattering between the object and the exit surface leads to the additional blurring in equation 13. As an example, for a high- D ($>10^3\ \text{e}^- \text{\AA}^{-2}$) TEM image of a gold nanoparticle in a $1\text{-}\mu\text{m}$ -thick water layer, for which the resolution is limited by C_c rather than by the SNR, equation 7 predicts a resolution of $3\ \text{nm}$. However, with the object at the top of the water layer, equation 13 predicts a resolution of only $\sim 9.8\ \text{nm}$ owing to beam broadening occurring between the object and the beam exit side of the sample and

consequent blurring of the image. It is therefore worth designing the experiment so that for TEM, the region of interest is close to the lower (exit) boundary of the liquid. For example, electrodes should be patterned on the exit window, and nanoparticle growth on the exit window will be imaged with the best resolution. However, beam blurring rapidly becomes unimportant for thin water layers. For example, $x_{25-75} = 3.5\ \text{nm}$ and $0.3\ \text{nm}$ for $z = 0.5\ \mu\text{m}$ and $0.1\ \mu\text{m}$, respectively.

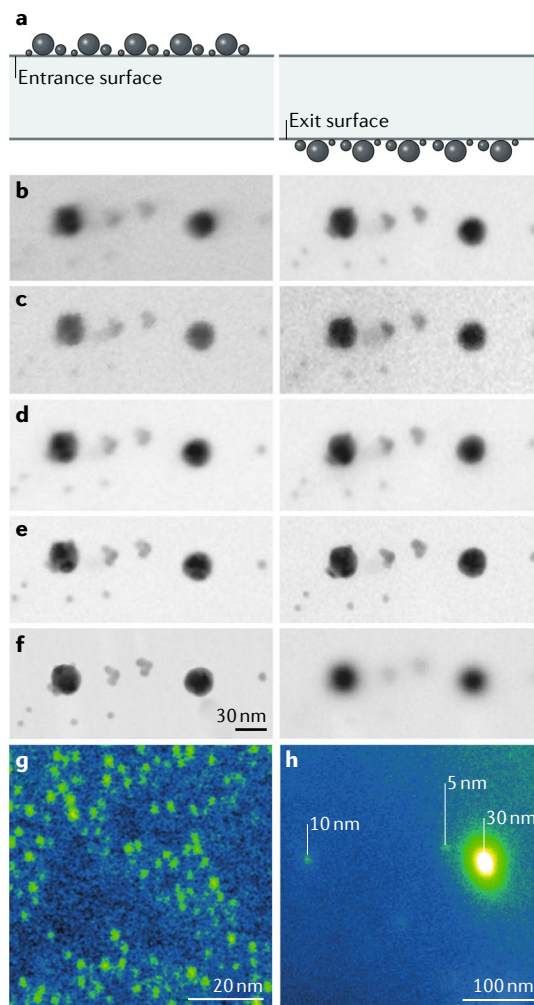


Fig. 3 | Resolution in different imaging modes. Panel a shows an illustration of two samples comprising gold nanoparticles $5\text{--}30\ \text{nm}$ in diameter on the electron entrance (left) and exit (right) surfaces of a $500\ \text{nm}$ amorphous silicon nitride layer. Panels b–f show images of the two samples illustrated in panel a acquired using uncorrected transmission electron microscopy (TEM) (panel b), energy-filtered TEM (EFTEM) (panel c), spherical aberration (C_s)-corrected TEM (panel d), C_s and chromatic aberration (C_c)-corrected TEM (panel e) and uncorrected scanning TEM (STEM) (panel f). All images were obtained at $200\ \text{keV}$. Panel g shows a dark-field STEM image of a liquid sample containing gold nanoparticles with an average diameter of $1.4\ \text{nm}$ above a liquid layer with a thickness of $3.3\ \mu\text{m}$. Panel h shows a similar dark-field STEM image of gold nanoparticles with diameters of $5\ \text{nm}$, $10\ \text{nm}$ and $30\ \text{nm}$ below a $1.3\text{-}\mu\text{m}$ -thick water layer. Panels a–f are adapted with permission from REF.⁹², Elsevier. Panels g and h are adapted with permission from REF.⁸, Elsevier.

Practical considerations. Understanding the relationship between experimental design and resolution is useful for evaluating one's own or published data, and several factors are worth considering.

Liquid thickness needs to be optimized for the material or process under study. In microfabricated liquid cells, the liquid is typically substantially thicker in the centre of the liquid cell than at the edges, as the windows deflect outwards because of the pressure difference across them. The liquid thickness also varies in graphene liquid cells. Choosing to image at the thinnest region of the liquid layer maximizes image resolution but may not replicate physical phenomena accurately in situ, such as those involving diffusion fields.

Window design is an important aspect of the experiment. In microfabricated liquid cells, the window deflection can be calculated from the dimensions, thickness and modulus of the windows. Deflection is minimized — and hence, resolution is improved — for stiff, thick and narrow windows or windows that are mechanically connected. Liquid cell design innovations are helping to address this issue, but constraints must still be balanced, such as thick windows reducing the resolution or narrow windows restricting the field of view. For thick liquid layers, choosing a thin window does not provide a substantial resolution benefit. For example, in a liquid cell filled with 1 μm of water, 50 nm silicon nitride windows contribute <10% to the chromatic blur. However, thin windows are more worthwhile if the liquid is less than a few hundred nanometres in thickness, as the relative contribution increases rapidly for thinner liquid layers.

The presence of bubbles has a pronounced influence on the achievable resolution. If a bubble forms as a result of radiolysis or precipitation of dissolved gases^{16,53,54}, the liquid may be present only as a thin wetting layer on the interior surfaces of the liquid cell. Such wetting layers still exhibit phenomena such as nanoparticle movement⁵⁵. Some published images that do not explicitly state a measurement of liquid thickness may have a high resolution because of a bubble and thus do not reflect the controlled physical surroundings intended for the experiment, that is, a full liquid layer.

The imaging of dynamic processes is particularly sensitive to radiation damage. In a hypothetical situation in which the sample is resistant enough to obtain atomic-level resolution in a single image with 0.3 nm detail, a resolution of only 1 nm can be achieved if the same dose is spread over a series of, for example, 10 images.

C_s correction in TEM of liquids

As beam sensitivity is often the factor limiting TEM resolution for liquids, it might be concluded that C_s correction is valuable only in restricted circumstances: it can improve the resolution only if the sample is not too thick and not beam-sensitive or if irradiation effects are the subject of the experiment. However, C_s correction has benefits other than resolution improvement, and these also apply when imaging dose-sensitive liquid samples. In the following, we consider not only resolution improvement but also delocalization, image

interpretability and depth resolution in the context of C_s -corrected TEM of liquids.

Spatial resolution improvement by C_s correction. Both hardware and software approaches have circumvented aberration and improved the resolution of modern TEMs. However, software techniques that reconstruct the exit plane wavefunction by combining information from multiple images^{56,57} are not optimal for liquid samples because of both dose sensitivity and the dynamic nature of the sample. By contrast, hardware correction of C_s (REFS^{58,59}) has been implemented in hundreds of modern TEMs that are compatible with liquid cell TEM sample holders. C_s -corrected liquid cell data have been obtained, for example, in experiments measuring beam-induced nanoparticle growth³. C_s correction has two immediate effects. First, the TEM resolution improves appreciably from $\sim 100\lambda$ to $\sim 40\lambda$. Resolution below 0.08 nm can be readily achieved for samples that can withstand the high electron densities used at such high magnification imaging — often $\gg 10^4 \text{ e}^- \text{ \AA}^{-2}$. Second, it is possible to choose a defocus at which a broad transfer band extends up to the information limit. This improves the point resolution and image interpretability by avoiding the high-frequency oscillations in the contrast transfer function that are observed in uncorrected TEM beyond ~ 0.2 nm resolution.

Delocalization. The oscillations of the transfer function lead to delocalization of information^{60,61}. Delocalization refers to the lateral displacement of high-resolution image detail by a distance that depends on spatial frequency, defocus and C_s . Delocalization effects are not readily apparent for a single crystal with uniform thickness and translational symmetry. However, discontinuities such as edges locally break the symmetry so that delocalization effects become visible: lattice fringes can be displaced significantly with respect to the true position of a nanocrystal. In uncorrected TEM, delocalization effects can usually be minimized only for a single spatial frequency at each defocus value. Thus, C_s correction improves image interpretability in the sub-nanometre resolution range. The effect of C_s correction on delocalization for a crystal edge in vacuum is clear (FIG. 4a,b), and an analogous effect is seen when nanoparticles are imaged in liquid (FIG. 4c,d). Many liquid cell experiments aim to study the solid–liquid interface. Avoiding delocalization increases the ability to interpret the fine detail often visible at nanoparticle surfaces and, similarly, would improve the interpretation of phenomena such as ordering within the liquid, expanding the prospects for extracting useful information from the observations.

Depth resolution in C_s -corrected imaging. An important goal in imaging liquid samples is to obtain structural information in the third dimension, along the beam direction. When objects are located at distinct depths, such as nanoparticles nucleating at the top and bottom windows of a closed cell, it is easy to determine the position of each object from the blurriness of the image, as discussed above. More generally, however, we wish to

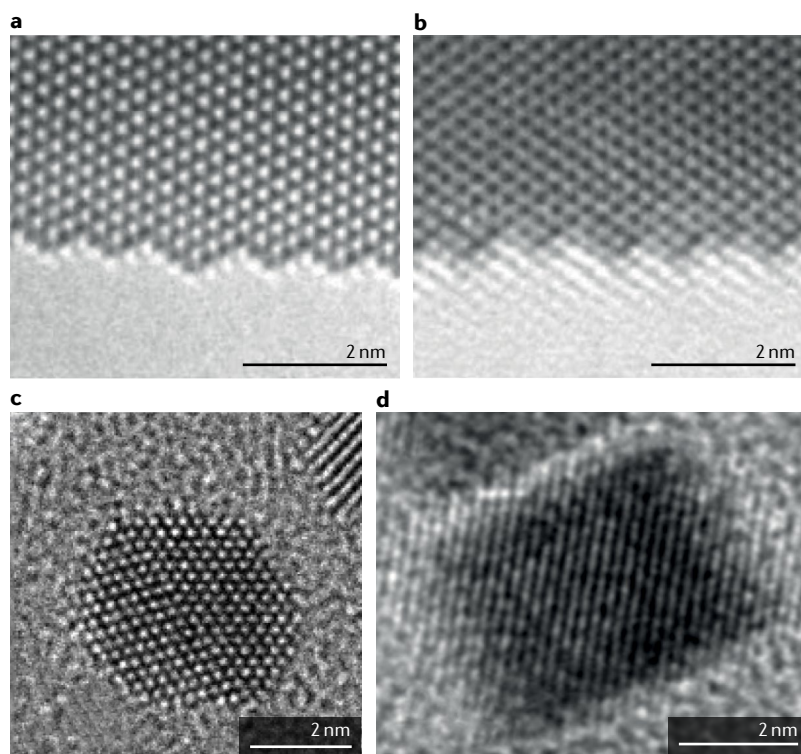


Fig. 4 | Effect of C_s correction in TEM. **a** | Transmission electron microscopy (TEM) image of a gold crystal at 200 keV with spherical aberration (C_s) correction. **b** | TEM image of the same sample as in panel **a** but without C_s correction. The images show that C_s correction decreases delocalization and increases image interpretability. Both images were obtained with the use of a monochromator¹²⁵. **c** | C_s -corrected image of a platinum nanoparticle in a graphene liquid cell during growth⁵. **d** | Uncorrected image of a platinum particle in a microfabricated liquid cell during growth¹³. Panels **a** and **b** are adapted with permission from REF.¹²⁵, Elsevier. Panel **c** is adapted with permission from REF.⁵, AAAS. Panel **d** is adapted with permission from REF.¹³, AAAS.

measure the vertical position and also the length in the beam direction of an arbitrary object within the liquid. C_s correction helps here; confocal imaging is possible because C_s correction enables larger convergence angles to be used and hence a smaller depth of focus, Δz , which scales with $2\lambda/\alpha^2$ (REF.⁶²). Improved optical sectioning has been demonstrated in C_s -corrected STEM^{62,63}. Typical values for non-corrected STEM are $\alpha = 9$ mrad and $\Delta z = 62$ nm for a beam energy of 200 keV, which may improve to $\alpha = 45$ mrad and $\Delta z = 2.5$ nm with C_s correction. The benefits for TEM have also been examined⁶⁴. Beam-tolerant liquid samples could provide an interesting opportunity to evaluate 3D imaging in both TEM and STEM.

Negative C_s imaging. Even in C_s -corrected imaging, the local image intensity still varies with defocus. Quantitative interpretation that relates contrast to structural features of the sample thus requires comparison with image simulations. However, the ability to tune C_s provides a powerful method for recording images that are easier to interpret without the need for simulations. In particular, setting C_s to be small and negative (the so-called negative C_s imaging mode (NCSI)) increases the contrast for low- Z objects^{65,66}. The ability to balance different symmetrical round aberrations using negative

aberration parameters increases the precision of composition and position measurements⁶⁷. In thin solid samples, NCSI has been used to measure local variations in atomic position with sub-5 pm precision⁶⁸. For liquid samples, the benefit of NCSI in the relevant resolution range is still an open question. It will be exciting to see experimental work using this imaging mode. For example, NCSI could, in principle, enhance dose efficiency through its improved contrast. A possibility could be to measure the 3D morphology of an individual nanoparticle from a single image obtained in, for example, a thin graphene liquid cell.

In situ experiments and the lifetime of the corrected state. When probing dynamic processes, the improved interpretability of C_s -corrected imaging is useful in solid samples^{69,70}. In liquid samples, studies of dynamic processes similarly benefit from C_s correction⁵. However, recording a time series requires the electron optical system to remain aligned for perhaps 10–20 min. This leads us to consider the lifetime of an aligned optical state. The stability of the electron optics of a microscope is generally determined by the thermal and environmental stability of the power supplies and lenses. A benefit of aberration-corrected electron microscopes is that the optics and electronics are generally more stable than in non-corrected and older systems. At present, the typical lifetime of a state that preserves image detail up to the information limit is on the order of a few minutes⁷¹. However, it is possible to trade resolution for stability⁷², and the lifetime scales approximately quadratically with resolution. A balance can therefore be chosen between a resolution that is sufficient to measure the objects under observation and a lifetime that is sufficient for the process under study. In the future, continuous aberration control is an interesting possibility that could enable even longer experiments in dose-tolerant samples.

C_c correction in TEM of liquids

Relatively few instruments worldwide possess C_c correction⁷³. However, for those that do, the results are significant: compared with C_s correction alone, C_c correction extends the information limit, offers increased contrast transfer for fine image details, reduces defocus spread and improves spatial resolution to values beyond $\sim 20\lambda$. C_c correction is especially effective at lower accelerating voltages (discussed below) and also when the electrons that form the image exhibit a broad range of energies^{74–77}. As an example, for the C_c and C_s (C_s/C_c)-corrected PICO TEM at the Ernst Ruska-Centre in Jülich, Germany, the defocus spread is reduced by more than a factor of ten compared with uncorrected TEM, and the resolution is 50 pm at 200 keV and 90 pm at 50 keV. For TEM of liquids, the resolution improvement in itself is difficult to exploit, as 50 pm resolution is unlikely to be realized in a typical sample. Instead, we anticipate that other capabilities of a C_c -corrected instrument will be more useful. The improved imaging of thick samples may be the most important benefit of C_c correction; conversely, for very thin samples, low-keV C_c -corrected imaging provides opportunities to retain resolution while reducing beam damage. Energy-corrected imaging may turn out to be

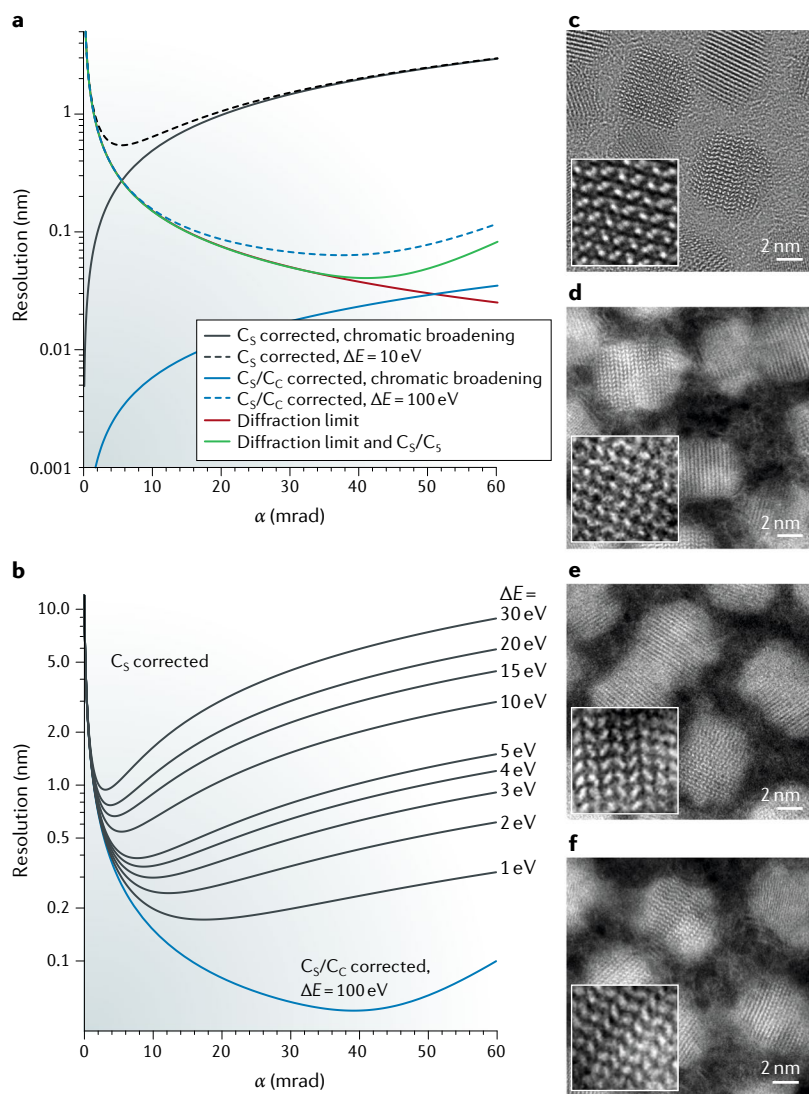


Fig. 5 | Influence of C_c correction on energy-filtered TEM. **a,b** | Calculations of the effect of energy spread (ΔE) and chromatic aberration (C_c) correction on image resolution. The calculations are based on expressions that are valid under the assumption that inelastic scattering fills the collection angle uniformly¹²⁶. Panel **a** shows a plot of spatial resolution in energy-filtered transmission electron microscopy (EFTEM) with a field emission gun at 200 keV as a function of the collection semi-angle, α , when there is a spread in energy. Compared with the resolution of a spherical aberration (C_s)-corrected microscope for a large energy-selecting slit width (ΔE) of 10 eV, C_s and C_c (C_s/C_c) correction improves the resolution even when ΔE is large, 100 eV. The contributions of chromatic broadening (black and blue solid lines) and the diffraction limit (solid red line) are also shown. The total resolution is the sum of residual delocalization and chromatic broadening. The residual delocalization (solid green line) is shown for an aberration-corrected instrument with an ideal monochromatic source and includes the diffraction limit. In the example shown, a non-zero C_s is used to balance a fifth-order spherical aberration, C_s , of -4 mm for optimum phase contrast, with the reciprocal information limit α/λ (where λ is the electron wavelength). Panel **b** shows the C_s -corrected, $\Delta E = 10$ eV plot along with plots for several other ΔE values, as well as a plot for C_s/C_c correction for $\Delta E = 100$ eV. C_s -corrected resolution degrades as ΔE increases, whereas for C_s/C_c correction the resolution is independent of ΔE . **c–f** | Experimental demonstration of maintained resolution in C_s/C_c -corrected imaging for large atomic weights in a solid sample consisting of CdSe nanoparticles on a carbon support. Images were recorded on the PICO TEM at the Ernst Ruska-Centre in Jülich, Germany, at 80 keV, with a 20 s exposure time and no objective aperture. Panel **c** shows a high-resolution TEM image, and panels **d–f** show EFTEM images recorded at a large energy loss of 70 eV with $\Delta E = 10, 20$ and 30 eV, respectively. The images include contributions from plasmon losses and one of the strong core-shell energy losses (the Se M_{45} core loss). Adapted with permission from REF.⁸⁶, Cambridge University Press.

more dose-efficient than conventional energy filtering while providing an even better image resolution. More speculatively, the use of C_c correction may enable in situ experiments that require extensive space in the sample area and improvement of material contrast using specialized imaging modes. We discuss these benefits in the following sections.

Improved energy-filtered imaging. C_c correction improves image resolution in EFTEM^{76,78,79}. This is because in EFTEM, electrons that have lost a particular amount of energy are selected by passing through a slit. The slit has a finite width, ΔE , which is a few eV to tens of eV, and the energy range of electrons that pass through the slit leads to a spread in defocus in the image. Without C_c correction, a larger ΔE results in a greater fraction of the incident beam being used to form the image and hence more dose-efficient imaging but larger chromatic blur. Thus, there is a trade-off between dose efficiency and resolution. In a C_c -corrected TEM, large energy windows and large objective apertures can be used because electrons with all energies are focused together. The energy-selecting window can be extended to tens of eV in width, enabling dose-efficient imaging without compromising spatial resolution (FIG. 5a,b).

Without C_c correction, the chromatic blur of equation 7 limits the spatial resolution of EFTEM to more than a few angstroms (and nanometres for thicker samples), even when the energy-selecting slit width and collection semi-angle are small. C_c correction reduces the chromatic blur by more than two orders of magnitude and provides sub-angstrom resolution even at the largest slit width and collection angle, with the additional benefit of good SNR^{78,79} (FIG. 5c–f). The importance of dose-efficient imaging in most liquids underscores the necessity of future experiments to evaluate the extent to which C_c correction improves EFTEM of liquid samples.

Improved imaging for thick samples. In the absence of C_c correction, the resolution in thick samples is limited by chromatic blur caused by multiple inelastic scattering events. One strategy for optimizing the image quality is to use a narrow energy-selecting slit to reduce the chromatic blur, thereby improving the resolution and depth of focus. However, the narrow slit reduces the dose efficiency. A better balance between resolution and dose is obtained if the energy-selecting slit is centred not on the zero-loss peak but on the most probable energy loss that the primary electrons undergo for that sample thickness⁸⁰. As an example, such energy-filtered imaging is applied to a solid, thick sample of whole mount macrophage cells⁸¹ in FIG. 6a. The image resolution is as high as 2.5 nm in this sample despite its thickness of well over 2 μm ; however, depth effects are visible, as the resolution is poorer for nanoparticles located at the top of the sample⁸⁰.

In a C_s/C_c -corrected microscope, all electron energies and angles are in focus. Almost all the single inelastically scattered electrons can be used to form the image, as these typically lose energy without changing their direction significantly. Thus, there is a notable advantage

in C_s/C_c -corrected imaging of dose-sensitive thick samples, compared with energy filtering alone. With C_s/C_c correction, the spatial resolution obtained for thick samples is similar to that obtained for EFTEM but with the advantage of higher dose efficiency (FIG. 3c–e; FIG. 6b,c). A related benefit of C_s/C_c correction is that regions of the sample with different thicknesses are all imaged at an optimal defocus without the need to adjust for changes in the most probable energy loss⁸⁰.

C_s/C_c -corrected imaging with a phase plate. Phase plates were developed to increase image contrast and hence improve the dose-limited resolution of low-contrast and beam-sensitive biological samples^{82,83}. The phase plate improves contrast transfer at low spatial frequencies by changing the phase of the central beam with respect to the scattered beams. High contrast can be obtained without needing a large defocus, and high resolution can be obtained without reconstructing a through-focal series with the consequent high dose. Phase plates are not yet widely used in liquid cell TEM, but we would expect significant benefits for imaging low-contrast and beam-sensitive liquid samples at the lowest dose possible.

Phase plates are even less commonly used in aberration-corrected instruments. However, the combination should in principle be valuable for imaging liquids. C_s correction plus a phase plate should theoretically produce the maximum possible phase contrast⁷⁵. The corrector and phase plate can be optimized together for the frequency spectrum of the object. This flexibility should improve the resolution of phase-contrast imaging by enabling imaging close to focus while maintaining the full object contrast. C_c correction should increase performance further because it will compensate for the loss of coherence owing to inelastic scattering in the sample and phase plate. As with other applications of C_c correction, the greatest benefits will be seen for thicker samples that substantially exceed the inelastic mean free path in thickness, common in imaging liquids. The dose

efficiency will be higher than is possible from a combination of a phase plate and zero-loss filtered imaging. We are not aware of published results in this area and anticipate exciting advances in the future.

C_s/C_c -corrected holography in liquids. Lorentz imaging and holography in liquids are possible despite the difficulty of obtaining a suitable reference beam. Off-axis electron holography has been used, for example, to probe magnetic structure within cells of a magnetotactic bacterium enclosed in a liquid cell⁸⁴. Data were acquired in Lorentz mode (FIG. 7) using an electron biprism and a direct-detection camera to increase the fringe contrast at doses similar to those used in conventional TEM. Holography has also been applied to study electron-beam interactions with ionic liquids in an open cell geometry⁸⁵.

C_s/C_c correction would improve the resolution in studies of liquid samples, for example, liquids containing magnetic nanostructures. In Lorentz mode, the TEM objective lens is switched off to create magnetic-field-free conditions. C_s correction has already been used to mitigate the resulting resolution loss, achieving a spatial resolution better than 0.5 nm in the corrected Lorentz imaging of conventional samples at both low⁸⁶ and high⁸⁷ voltages. C_s/C_c correction would improve the resolution further, especially at lower voltages and for thick samples. In the future, it may be possible to use C_c -corrected holography to image magnetic fields originating from the presence of ferromagnetic materials in liquids with close to atomic spatial resolution.

Low-energy C_s/C_c -corrected TEM. A further possible advantage of C_s/C_c correction is the ability to acquire TEM images with high resolution even at low beam energy, perhaps as low as 20 keV (REF.⁸⁸). To exploit the full advantage of C_c correction at this beam energy, the sample must be very thin to achieve sufficient transmittance. For liquids, a possible solution is to use a graphene liquid cell¹¹. Low-energy C_s/C_c -corrected imaging of such samples enables a new range of experiments

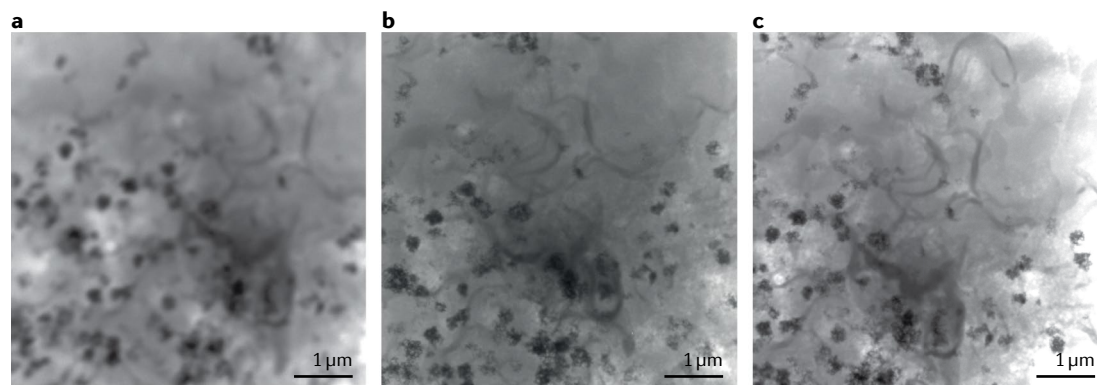


Fig. 6 | **Bright-field TEM images of a thick sample of a whole mount macrophage cell.** **a** | Energy-filtered, spherical aberration (C_s)-corrected overview transmission electron microscopy (TEM) image showing low-density lipoprotein-coated gold nanoparticles uptaken by a macrophage cell and assembled in clusters. **b** | A chromatic aberration (C_c) and C_s -corrected image of the area imaged in panel **a**. **c** | The same image as shown in panel **a** but refocused to the most probable energy loss. The image in panel **b** has a similar resolution to the image in panel **c** but was obtained without excluding electrons from image formation and without adjusting the focus to a certain energy loss. Bright-field TEM images were recorded at 300 keV with the PICO C_s and C_c -corrected TEM at the Ernst Ruska-Centre in Jülich, Germany. The exposure time was 5 s. Adapted with permission from REF.⁸⁶, Cambridge University Press.

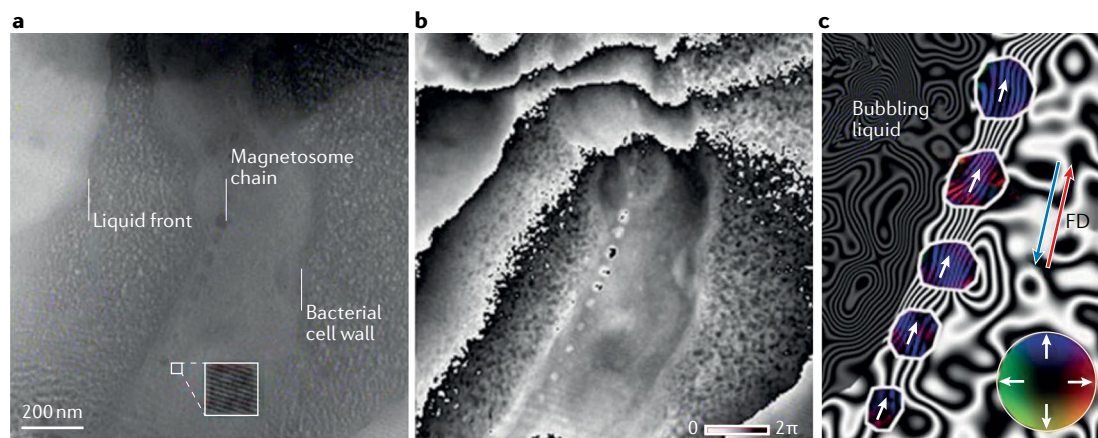


Fig. 7 | Electron holography and associated analysis of a hydrated bacterial cell. **a** | Off-axis electron hologram of a hydrated magnetotactic bacterial cell between silicon nitride windows. The magnified region in the inset shows well-resolved interference fringes with a spacing of 5.6 nm. **b** | Phase of the electrons at each point in the image, calculated from the hologram in panel **a**. A visible phase change is caused by the magnetite chain in the magnetotactic bacterial cell, enabling the magnetic properties of the chain to be inferred. **c** | Magnetic induction map of part of the magnetite chain, obtained from holograms recorded under two different magnetic field directions (FDs). The black phase contours show the magnetic contribution to the measured phase shift and have a spacing of 0.098 ± 0.001 rad. The magnetite nanocrystals are outlined in white. The direction of the measured projected in-plane magnetic induction is shown using arrows and the colours in the inset colour wheel. Adapted with permission from REF.⁸⁴, The Royal Society Publishing; permission conveyed through Copyright Clearance Center, Inc.

because the beam energy is below the knock-on damage threshold of both bulk and surface atoms for most materials, including carbon-based materials, and the contrast obtained is higher than that at 200 keV. We speculate that an optimized dose–resolution balance will be found for beam-sensitive liquid samples at, for example, 20 keV.

C_s/C_c -corrected imaging for novel liquid imaging modes. The most speculative benefit of C_s/C_c correction for liquid samples arises because the microscope design can be completely reimaged if C_c is zero. At present, high resolution is achieved by choosing a small pole-piece gap (for example, <2 mm) to reduce the C_c coefficient of the lens. With C_c correction, a wider pole-piece gap is possible while still maintaining high resolution. The wide gap provides space for bulky holders, detectors and other components around the sample. For liquid samples, possibilities of interest include correlative imaging, which involves simultaneous use of other microscopies; light stimulation by fibre optics or lasers; in situ irradiation by ion beams or other radiation; application of magnetic fields; complex liquid pumping systems; and accurate probes to measure or calibrate parameters such as temperature, window deflection or liquid chemistry. No dedicated C_c -corrected, large pole-piece gap in situ instrument exists, but future opportunities are compelling.

Spatial resolution in STEM of liquids

In STEM, as for TEM, the resolution for thin and stable solid samples depends on the electron optics, specifically the STEM probe size, which is of the order of 0.2 nm in uncorrected instruments. However, the resolution for more typical dose-sensitive liquid samples is limited by SNR and, for thicker samples, by beam blurring. In the following, we therefore consider both acceptable dose

and imaging mode, distinguishing between the cases of dark-field and bright-field STEM imaging of objects in liquid.

SNR-limited resolution in STEM. For objects at the beam entrance side of the specimen, imaged with the highest spatial resolution, the small amount of probe broadening due to the window can be neglected. The resolution is then limited by the achievable SNR, which in turn depends on the contrast and acceptable dose of the sample. To satisfy the Rose criterion, an object must be large enough to be detectable at a certain dose within a liquid layer of certain thickness and scattering properties.

We first consider the case of standard annular dark-field imaging conditions^{4,8}. Here, contrast is generated because the detector collects electrons that are elastically scattered out of the primary beam above a given semi-angle β . If there are N_0 electrons in the primary beam in each pixel (a function of probe current and dwell time), the fraction N/N_0 of electrons scattered into the detector is given by^{4,21}:

$$N/N_0 = 1 - \exp\{-t/l(\beta)\} \quad (14)$$

where $l(\beta)$ is analogous to $l(\alpha)$ defined in equation 8 but with semi-angle β . To a good approximation, $\sigma(\beta)$ is proportional to $Z^{4/3}$ (see Supplementary information). Using dark-field contrast, high- Z nanoparticles can be imaged with strong contrast even in liquid layers that are several micrometres thick⁴. For typical values⁴ of $\beta = 70$ mrad, $E = 200$ keV and mean free paths $l_w = 10.3$ μm and $l_o = 73$ nm for water and gold, respectively, we calculate the SNR for dark-field conditions similarly to the bright-field calculations for TEM (equations 8–11). The signals in the annular dark-field detector at the object

and in the background are given by equations 15 and 16, respectively⁴.

$$N_{\text{signal}}/N_0 = 1 - \exp\{-[t_0/l_o(\beta) + (t-t_0)/l_w(\beta)]\} \quad (15)$$

$$N_{\text{bkg}}/N_0 = 1 - \exp\{-t/l_w(\alpha)\} \quad (16)$$

To calculate the thickness of a gold nanoparticle that would be detectable above the background, we use the SNR limit of equation 11, a linear approximation assuming⁸ $t \ll t_0$ and $d_{\text{STEM}} = t_0$:

$$d_{\text{STEM}} = 3l_o(t/l_w N_0)^{1/2} \quad (17)$$

Equation 17 suggests that a gold nanoparticle with a 1 nm diameter can be resolved on top of a water layer of 5 μm using a probe current of 0.5 nA and a pixel dwell time of 10 μs . This is a remarkable result and is consistent with experimental data^{4,8} (FIG. 2).

If we now wish to express d_{STEM} explicitly as a function of D , an approximate solution is obtained by eliminating N_0 in equation 17 (similar to the approach used to derive equation 12) by using $N_0 = D(d_{\text{STEM}}/2)^2$. This leads to⁶:

$$d_{\text{SNR}} = \sqrt{\frac{6l_o}{l_w - l_o}} \left(\frac{tl_w}{D} \right)^{1/4} \quad (18)$$

The achievable spatial resolution thus depends on $D^{1/4}$ (REF.⁶). Therefore, achieving higher resolution in such samples is only possible at the cost of high electron doses. However, low-dose imaging is feasible if the resolution requirements can be relaxed.

Equations 17–18 involve several approximations and also neglect scattering in the windows. More precise calculations are possible through numerical solving and give similar results for the conditions under which the approximations apply⁶. Monte Carlo simulations provide the most precise calculation of the sample-dependent resolution and are not difficult to accomplish^{8,9}.

Achievable resolution. The achievable resolution for STEM was calculated at optimized settings for samples containing carbon and gold nano-objects (FIG. 2) by solving equations 11, 15 and 16 numerically. The results show that TEM is best for low- Z materials, such as carbon, in thin liquid layers, but STEM provides higher resolution at thicknesses at which phase contrast no longer applies. STEM provides higher resolution for high- Z materials, as expected from the strong Z -contrast imaging it provides. The benefits are particularly striking for high- Z nanoparticles in very thick liquid layers, for which a resolution of a few nanometres is possible in 10 μm of liquid at reasonably low D . These calculations are consistent with experimental data for imaging nanoparticles at different dose levels^{8,9,90}. Atomic resolution has been shown for STEM imaging of platinum nanoparticles¹⁶, and similar to TEM, the equations based on imaging single objects predict a lower resolution (higher value) than the resolution measured from lattice fringes.

Probe broadening in STEM. Probe broadening occurs because elastic scattering of the beam by the sample increases the probe diameter as the beam passes through the sample²¹. This effect is similar to the image blurring in TEM described by equation 13 and can limit the resolution possible for thick liquid samples^{8,91}. For STEM, the highest resolution is achieved for objects at the electron-beam entrance side of the sample. This is shown experimentally in a model sample consisting of gold particles on a thick amorphous film⁹² (FIG. 3f) and in a liquid sample containing gold particles above or below a thick water layer⁸ (FIG. 3g,h). Changes in spatial resolution (at a fixed electron dose) are visible as a function of the liquid thickness, with beam broadening starting to limit the resolution for nanoparticles below, typically, 1 μm of liquid.

Bright-field STEM. Bright-field STEM is an imaging modality that suffers less from beam broadening than the dark-field mode because scattering events at low angles do not substantially blur the probe. Bright-field STEM is therefore particularly advantageous when imaging thick samples. If some spatial resolution is sacrificed by reducing the beam opening angle, this can increase the focal depth so much that the entire thickness is imaged in focus^{93,94}. This has already proved beneficial for imaging dose-sensitive cryo sections up to 1 μm thick⁹⁵. The same effect can perhaps be used to improve the resolution in liquid cell bright-field STEM if the experimental settings are optimized⁶. An important recent advance is the development of segmented bright-field detectors that can be configured to obtain STEM bright-field phase contrast with increased detection efficiency⁹⁶. Pixelated detectors should lead to further improvements in detection efficiency in all STEM imaging modes.

C_s correction in STEM. C_s -corrected STEM has been applied to image nanoparticles in liquid^{39,97}, to write patterns in beam-sensitive solutions of metal ions⁹⁸ and to image individual molecules of ferritin and obtain information about chemical bonding⁹⁹. These examples illustrate three key consequences of C_s correction in STEM: improved spatial resolution by concentrating the beam current into a smaller probe than is possible in uncorrected STEM, increased SNR and faster compositional analysis by providing larger current in a probe of the same size as in uncorrected STEM.

In terms of minimizing probe size, C_s correction enables the formation of a probe of <0.1 nm. This improves the resolution but can be used only when the sample is highly dose-tolerant. For example, imaging thin solid samples with sub-angstrom resolution requires high-dose conditions, such as a 50 pA probe current, a 10 μs dwell time, a probe size of <0.8 \AA (REF.⁷) and hence an electron density of $\sim 10^4 \text{ e}^- \text{\AA}^{-2}$. Some solid samples can withstand such a high D , but we would expect strong beam effects in liquids. A key application of C_s correction in STEM of liquids may exist at the other end of the resolution scale. Instead of aiming for the highest spatial resolution, the operator could adjust the microscope to provide as much current as possible in a probe of reasonable size, for example, 0.5 nm. This would be useful for optimizing temporal resolution or compositional analysis.

C_s -corrected STEM has a second advantage: high resolution can still be achieved even at higher beam currents because larger beam-convergence angles are possible than in non-corrected STEM. Eventually, the fifth-order spherical aberration, C_s , becomes the limiting factor, but a beam current of several tens of nA is possible for sub-nanometre resolution¹⁰⁰. In practice, this type of resolution–beam current balance is commonly used in uncorrected STEM of liquid samples to optimize the information obtained for a given dose. A balance is achieved by adjusting towards smaller beam opening angles so that diffraction broadens the probe or by imaging slightly out of focus.

A third benefit of C_s -corrected STEM has already been discussed for TEM: the prospect of optical sectioning owing to the highly decreased focal depth^{63,101}. Combining a limited tilt series with a focal series has been shown to reduce the missing-wedge problem¹⁰² in tomography and may find application in 3D measurements in liquids.

Temporal resolution in liquids

Sequential images provide a powerful tool to measure kinetics during reactions, to detect transient intermediate states and to probe the response of a material to changes in the environment, such as temperature or field. Many in situ liquid cell electron microscopy studies acquire image series for such purposes. However, temporal resolution has two other benefits that are

particularly valuable for liquid samples: reducing the effects of the random motion of objects within a liquid and minimizing beam-induced artefacts through dose fractionation. The options available for recording time series range from video format (30 images per second, each of 480×640 pixels) to direct-detection cameras that can offer millisecond frame times. Increasing the image acquisition speed for a similar SNR per image implies that the electron flux has to be increased by using more current. A given dose is thus delivered more quickly to the sample. As discussed above, both total dose and dose rate affect the response of the sample to irradiation^{36,40}. Thus, a balance must be set between the spatial resolution required, the number of images recorded during the experiment, the temporal resolution and both the dose and dose-rate tolerance of the sample.

Conveniently slow Brownian motion. Depending on the image resolution required, an object of interest, such as a nanoparticle in a liquid, must move less than, for example, ~ 1 nm while the image is recorded. Yet, Brownian motion is expected to move nanoparticles much further within a typical image acquisition time. We can estimate the average length, Δx , that particles travel in time interval $\Delta \tau$ via Brownian motion using the following relation¹⁰³:

$$\Delta x = (k_B T \Delta \tau / 3\pi\eta r)^{1/2} \quad (19)$$

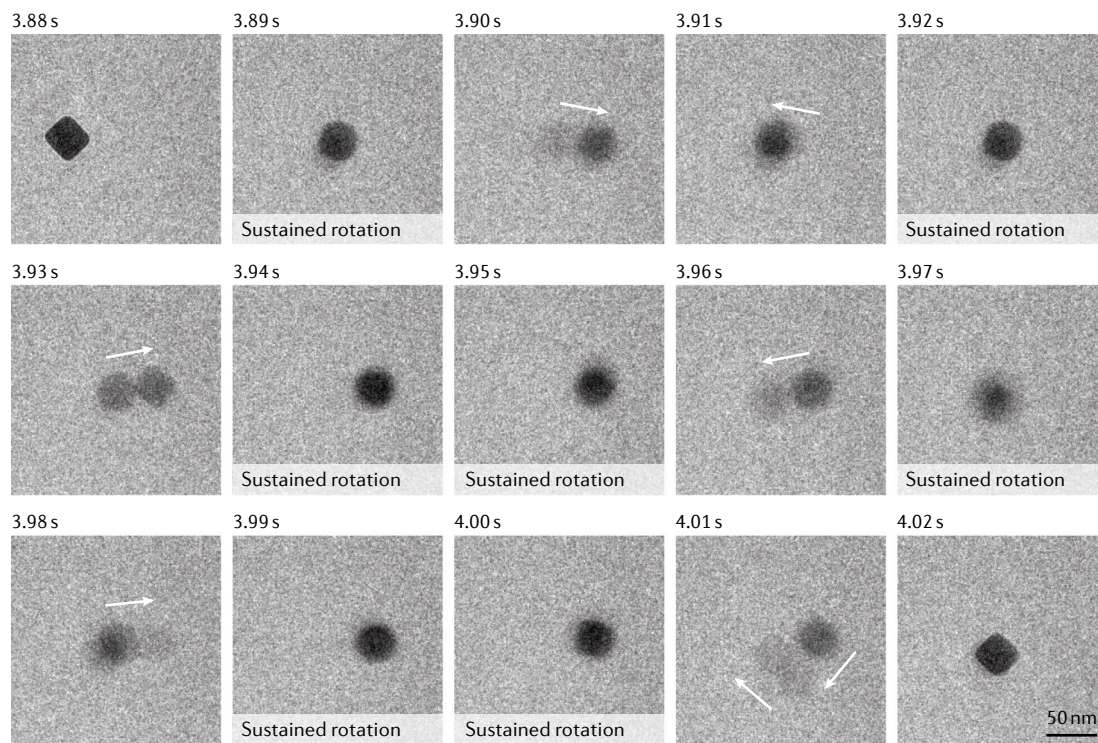


Fig. 8 | **In situ TEM of nanocube rotation.** Transmission electron microscopy (TEM) images extracted from a movie showing motion of a gold nanocube with a 15 nm radius coated with cetyltrimethylammonium bromide in a 70-nm-thick water layer. Images were acquired under $50 \text{ e}^- \text{ \AA}^{-2} \text{ s}^{-1}$ irradiation, at 100 frames per second and using zero-loss filtering. Jiggling, rotation and occasional long displacements of tens of nanometres (highlighted with arrows) occur within individual 10 ms frames. Frames such as the one at 3.93 s also suggest rotations occur during translation steps. Adapted with permission from REF.¹⁰⁵, American Chemical Society.

where k_B is Boltzmann's constant, T is the temperature, η is the viscosity of the liquid and r is the particle radius. For a nanoparticle with a 10 nm radius in water with $\eta = 8.9 \times 10^{-4} \text{ kg s}^{-1} \text{ m}^{-1}$ and at room temperature, we obtain $\Delta x = 7 \text{ nm}$ within $1 \mu\text{s}$. In other words, Brownian motion would be expected to prevent nanometre-level imaging of small particles for acquisition rates of even a few hundred images per second^{104–106}. Slower image acquisition is acceptable only for larger particles or structures attached to the liquid cell walls or for situations requiring lower resolution^{106,107}.

Despite these expectations, from the first reports of nanoscale resolution obtained on small particles in liquid^{4,9}, it became clear that good resolution was being obtained even without ultrafast image acquisition. For example, during acquisition of 100 images per second of a gold nanocube with a 15 nm radius in water (FIG. 8), many images show reasonable resolution, although motion is visible in others¹⁰⁵. A nanoparticle with this radius would be expected, from equation 19, to travel $\sim 6 \mu\text{m}$ during the 0.01 s image acquisition time, which is much farther than observed in FIG. 8. It is also possible to study the dynamics of moving nanoparticles over a longer timescale (FIG. 9). In these experiments, the motion of gold nanoparticles close to the silicon nitride window was observed to be three orders of magnitude slower than expected from Brownian motion⁵⁵. Similar effects have been observed in many liquid samples^{41,55,105,108–111}. The physics behind this exceptionally slow motion compared with Brownian motion is still unresolved, with ongoing discussions of the effects of liquid ordering near the interface¹¹², electric fields induced by electron-beam irradiation¹¹³, partial binding⁹ and beam-affected trapping and de-trapping of particles at the surface¹¹⁴. The practical outcome is that high-quality observations seem possible in liquids at reasonable temporal resolution, despite expectations based on Brownian motion.

Temporal versus dose-limited resolution. Recording images at high temporal resolution creates a conflict with noise-limited spatial resolution requirements. Increasing the electron flux to maintain the dose per

image means that the sample will exceed its acceptable dose more rapidly; alternatively, at fixed electron flux, reducing the exposure time will reduce the number of counts in the image until eventually the spatial resolution becomes limited. Although this is a fundamental limitation, there is room for improvement. It is worth considering whether the dose can be distributed over time to match the phenomenon under study; for example, a process that slows down with time could be imaged more slowly at later times to reduce the total dose to the sample without losing much information. More efficient detectors provide a straightforward way to collect more images without increasing the dose to the sample. Direct-detection cameras using thinned sensors show excellent performance⁴². With direct-detection cameras, the noise is reduced owing to the elimination of the fibre optic link used conventionally, and the detector quantum efficiency is increased over a wide frequency range. Moreover, both the fill factor and duty cycle are 100%; thus, virtually all electrons are counted. Image acquisition at, for example, 400 frames of $2,000 \times 2,000$ pixels per second is a significant improvement over standard video acquisition. Along with the high efficiency and low noise, a great benefit of these types of detectors is the ability to carry out dose fractionation. However, a challenge is the difficulty of handling the data. For example, 400 frames of $2,000 \times 2,000$ pixels per second equates to more than 3 GB s^{-1} (with each pixel value stored in 16 bit), which is comparable to the data rate from CERN. Data compression and automatic image processing therefore become necessary to handle the experimental data.

If higher temporal resolution is required, dedicated TEM systems can be used. These involve the principle of dynamic TEM (DTEM)¹¹⁵, in which a laser triggers a burst of imaging electrons and a simultaneous stimulus to the sample. Pulse-probe measurements of repeated processes are possible^{104,116}. These specialized DTEM instruments have been used with liquid cells to study processes such as light-induced nanoparticle growth¹¹⁷.

Time-resolved STEM is an imaging modality that is not often used, and most scanning units are not designed for high speed. In particular, the typical scanning saw-tooth

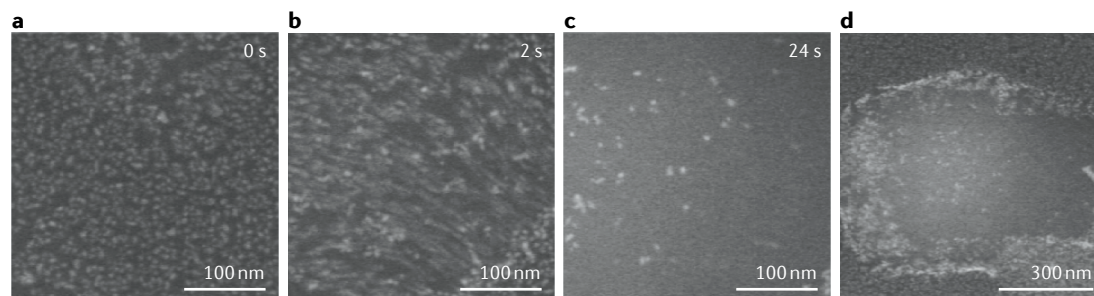


Fig. 9 | **Time-resolved STEM imaging of gold nanoparticles moving in liquid.** Each image represents a running average of eight frames recorded at video frequency (that is, with a 0.3 s time interval). **a** | Scanning transmission electron microscopy (STEM) image of 5 nm gold nanoparticles taken at the onset of movement. **b** | Image of the same location after 2 s exposure to the beam; motion has just begun. Movement of the nanoparticles is apparent from the $\sim 0.1 \mu\text{m}$ streaks. Note that equation 19 predicts that these nanoparticles would travel $8 \mu\text{m}$ in water within 0.3 s, several orders of magnitude larger than is seen. **c** | Image in the same location after 24 s exposure. Most nanoparticles have left the field of view, and those that are visible do not move. **d** | Image of the remaining nanoparticles after zooming out, showing that the nanoparticles that had not been exposed to the electron beam had not moved. Adapted with permission from REF.⁵⁵, Elsevier.

signal requires a considerable fly-back time of hundreds of milliseconds. However, image series can be obtained to provide time-dependent Z-contrast information on phenomena such as nanoparticle motion or electrochemical growth^{39,55,112,118,119}. Changes in image intensity during the scanning of a single image have been used to provide sub-frame temporal resolution in measurements of ion concentration in solution¹²⁰. Many opportunities exist in this mostly unexplored territory of time-resolved STEM. For example, commercial STEM instruments readily operate with a pixel dwell time of 1 μ s. Instead of acquiring a large square image, it would be beneficial to acquire the smallest possible image and minimize fly-back time with optimized scanning schemes¹²¹. Without fly-back time, a scan unit could in principle acquire a 128 \times 128 pixel image in 18 ms. The dwell time could be reduced by using detection and readout optimized for high speed. It would be advantageous to increase the current per pixel to maintain sufficient SNR (for example, using the analytical mode instead of the imaging mode), for which C_s correction would be beneficial.

To increase acquisition speed even further, smart acquisition schemes can be used, such as those involving compressive sensing techniques⁴⁵. For STEM, electrostatic scan coils as used in SEM could in principle also be designed for higher accelerating voltage, or STEM-in-SEM can be used at higher speeds. It could also be possible to avoid scanning altogether and observe objects flying into and out of the liquid column irradiated with the electron beam. The resulting intensity versus time signal can be detected with (sub-)nanosecond temporal resolution using standard photomultiplier tubes, an interesting prospect for future investigations.

Finally, in seeking a solution to optimize the balance between dose and temporal and spatial resolution, a combination of microscopy modalities may turn out to be necessary, as has been shown already for correlative fluorescence and electron microscopy. One option is to combine cryo-electron microscopy methods with liquid cell electron microscopy¹²². Cryo-electron microscopy would provide high-resolution, static images of frozen structures, whereas the dynamic transition between these states would be examined in liquid at lower resolution.

Summary and outlook

Electron microscopy of liquids is capable of producing high-resolution information. It is possible to visualize the motion of nanoparticles and discriminate subtle details of materials and biological structures in the

liquid phase. Although thin liquid layers provide images with higher spatial resolution, thicker samples can provide a better model of bulk processes yet still maintain acceptable temporal and spatial resolution.

To understand the limits of spatial and temporal resolution in TEM and STEM of liquids, we have combined the ideas of aberration-limited and noise-limited spatial resolution with the maximum dose that a liquid sample can tolerate without damage and applied the concepts to thick samples that often have low contrast. In a general liquid imaging experiment, we suggest that resolution is most commonly constrained by dose limitations. For experiments that image biological materials, this is not a surprising outcome based on cryo-electron microscopy experience. However, even for less sensitive materials such as metal nanoparticles or thin films in an aqueous environment, beam effects can have a dominant role because of the sensitivity of the surrounding water to electron irradiation.

The benefits of C_s correction in TEM and STEM for imaging liquids include improved interpretability of images, reduced delocalization and smaller depth of field. Combined C_s/C_c correction offers improvement in the ability to image thick materials dose-efficiently, to acquire EFTEM images using large energy-selecting windows and to improve spatial resolution in possible future wide-gap microscopes designed for in situ experiments. However, these advantages must be balanced against the increased complexity and cost of aberration-corrected instruments.

As techniques for imaging liquids with electrons develop, we can expect to see improvements in the quality and quantity of information and in the matching of data with simulations and models. We anticipate that microscopes with C_s/C_c correction and energy-filtering capabilities will be applied more widely to liquid samples. We also expect that more general adoption of high-performance detectors, advanced image processing and high-speed STEM will make an immense difference to the practice of electron microscopy of liquids, improving SNR and enabling dose fractionation. As with all microscopy techniques, the early years have provided exciting and often qualitative information, and future developments promise exciting opportunities for quantitative analysis, modelling and prediction of materials properties and processes in liquid environments.

Published online 19 December 2018

- Ross, F. M. *Liquid Cell Electron Microscopy* (Cambridge Univ. Press, 2017).
- Ross, F. M. Opportunities and challenges in liquid cell electron microscopy. *Science* **350**, aaa9886 (2015).
This article discusses the range of problems accessible with closed liquid cell electron microscopy.
- de Jonge, N. & Ross, F. M. Electron microscopy of specimens in liquid. *Nat. Nanotechnol.* **6**, 695–704 (2011).
This article provides an overview of the breakthroughs in liquid cell electron microscopy in the 2000s that led to the current growth of the field.
- de Jonge, N., Peckys, D. B., Kremers, G. J. & Piston, D. W. Electron microscopy of whole cells in liquid with nanometer resolution. *Proc. Natl Acad. Sci. USA* **106**, 2159–2164 (2009).
This is the first demonstration of nanometre resolution in micrometre thick liquids containing a mammalian cell.
- Yuk, J. M. et al. High-resolution EM of colloidal nanocrystal growth using graphene liquid cells. *Science* **336**, 61–64 (2012).
This is the first demonstration of the high resolution possible with a graphene liquid cell.
- de Jonge, N. Theory of the spatial resolution of (scanning) transmission electron microscopy in liquid water or ice layers. *Ultramicroscopy* **187**, 113–125 (2018).
This article provides the theory needed to calculate the resolution for TEM and STEM of liquid samples.
- Nellist, P. D. et al. Direct sub-angstrom imaging of a crystal lattice. *Science* **305**, 1741 (2004).
- de Jonge, N., Poirier-Demers, N., Demers, H., Peckys, D. B. & Drouin, D. Nanometer-resolution electron microscopy through micrometers-thick water layers. *Ultramicroscopy* **110**, 1114–1119 (2010).
- Zheng, H., Claridge, S. A., Minor, A. M., Alivisatos, A. P. & Dahmen, U. Nanocrystal diffusion in a liquid thin film observed by in situ transmission electron microscopy. *Nano Lett.* **9**, 2460–2465 (2009).
- Williamson, M. J., Tromp, R. M., Verreken, P. M., Hull, R. & Ross, F. M. Dynamic microscopy of nanoscale cluster growth at the solid–liquid interface. *Nat. Mater.* **2**, 532–536 (2003).
This is the first demonstration of TEM and electrochemical control in a liquid cell constructed from silicon microchips with silicon nitride windows.

11. Textor, M. & de Jonge, N. Strategies for preparing graphene liquid cells for transmission electron microscopy. *Nano Lett.* **18**, 3513–3521 (2018).
12. Liao, H. G., Niu, K. & Zheng, H. Observation of growth of metal nanoparticles. *Chem. Commun.* **49**, 11720–11727 (2013).
13. Liao, H. G. et al. Facet development during platinum nanocube growth. *Science* **345**, 916–919 (2014).
14. Lehnert, T. et al. In situ crystallization of the insoluble anhydrite All phase in graphene pockets. *ACS Nano* **11**, 7967–7973 (2017).
15. Kelly, D. J. et al. Nanometer resolution elemental mapping in graphene-based TEM liquid cells. *Nano Lett.* **18**, 1168–1174 (2018).
16. Woehl, T. J. et al. Experimental procedures to mitigate electron beam induced artifacts during in situ fluid imaging of nanomaterials. *Ultramicroscopy* **127**, 53–63 (2013).
17. Bogner, A., Thollet, G., Basset, D., Jouneau, P. H. & Gauthier, C. Wet STEM: a new development in environmental SEM for imaging nano-objects included in a liquid phase. *Ultramicroscopy* **104**, 290–301 (2005).
18. Sugi, H. et al. Dynamic electron microscopy of ATP-induced myosin head movement in living muscle filaments. *Proc. Natl Acad. Sci. USA* **94**, 4378–4392 (1997).
19. Huang, J. Y. et al. In situ observation of the electrochemical lithiation of a single SnO₂ nanowire electrode. *Science* **330**, 1515–1520 (2010).
20. Kolmakov, A. in *Liquid Cell Electron Microscopy* (ed. Ross, F. M.) 78–105 (Cambridge Univ. Press, 2016).
21. Reimer, L. & Kohl, H. *Transmission Electron Microscopy: Physics of Image Formation*. (Springer, New York, 2008).
22. Egerton, R. F., Li, P. & Malac, M. Radiation damage in the TEM and SEM. *Micron* **35**, 399–409 (2004).
23. Schneider, N. M. in *Liquid Cell Electron Microscopy* (ed. Ross, F. M.) 140–163 (Cambridge Univ. Press, 2016).
24. Jiang, N. & Spence, J. C. H. On the dose-rate threshold of beam damage in TEM. *Ultramicroscopy* **113**, 77–82 (2012).
25. Frank, J. *Three-dimensional Electron Microscopy of Macromolecular Assemblies: Visualization of Biological Molecules in Their Native State* (Oxford Univ. Press, 2006).
26. Pierson, J., Sani, M., Tomova, C., Godsava, S. & Peters, P. J. Toward visualization of nanomachines in their native cellular environment. *Histochem. Cell Biol.* **132**, 253–262 (2009).
27. Hoenger, A. & McIntosh, J. R. Probing the macromolecular organization of cells by electron tomography. *Curr. Opin. Cell Biol.* **21**, 89–96 (2009).
28. Matricardi, V. R., Moretz, R. C. & Parsons, D. F. Electron diffraction of wet proteins: catalase. *Science* **177**, 268–270 (1972).
29. Mirsaidov, U. M., Zheng, H., Casana, Y. & Matsudaira, P. Imaging protein structure in water at 2.7 nm resolution by transmission electron microscopy. *Biophys. J.* **102**, L15–L17 (2012).
30. Keskin, S. et al. Visualization of multimerization and self-assembly of DNA-functionalized gold nanoparticles using in-liquid transmission electron microscopy. *J. Phys. Chem. Lett.* **6**, 4487–4492 (2015).
31. Hermansdörfer, J., Tinnemann, V., Peckys, D. B. & de Jonge, N. The effect of electron beam irradiation in environmental scanning transmission electron microscopy of whole cells in liquid. *Microsc. Microanal.* **20**, 656–665 (2016).
32. de Jonge, N. & Peckys, D. B. Live cell electron microscopy is probably impossible. *ACS Nano* **10**, 9061–9063 (2016).
33. Peckys, D. B. & de Jonge, N. in *Liquid Cell Electron Microscopy* (ed. Ross, F. M.) 334–355 (Cambridge Univ. Press, 2016).
34. Peckys, D. B., Mazur, P., Gould, K. L. & de Jonge, N. Fully hydrated yeast cells imaged with electron microscopy. *Biophys. J.* **100**, 2522–2529 (2011).
35. Liv, N. et al. Electron microscopy of living cells during in situ fluorescence microscopy. *ACS Nano* **10**, 265–273 (2016).
36. Abellan, P. et al. Factors influencing quantitative liquid (scanning) transmission electron microscopy. *Chem. Commun.* **50**, 4873–4880 (2014).
37. Yamazaki, T. et al. Two types of amorphous protein particles facilitate crystal nucleation. *Proc. Natl Acad. Sci. USA* **114**, 2154–2159 (2017).
38. Schneider, N. M. et al. Electron–water interactions and implications for liquid cell electron microscopy. *J. Phys. Chem. C* **118**, 22373–22382 (2014).
This study reports the modelling of radiolysis effects in water upon electron-beam irradiation.
39. Hermansdörfer, J., de Jonge, N. & Verch, A. Electron beam induced chemistry of gold nanoparticles in saline solution. *Chem. Comm.* **51**, 16393–16396 (2015).
40. Woehl, T. J., Evans, J. E., Arslan, L., Ristenpart, W. D. & Browning, N. D. Direct in situ determination of the mechanisms controlling nanoparticle nucleation and growth. *ACS Nano* **6**, 8599–8610 (2012).
41. Zheng, H. et al. Observation of single colloidal platinum nanocrystal growth trajectories. *Science* **324**, 1309–1312 (2009).
This is the first observation of nanoparticle growth using liquid cell electron microscopy.
42. Contarato, D., Denes, P., Doering, D., Joseph, J. & Krieger, B. High speed, radiation hard CMOS pixel sensors for transmission electron microscopy. *Phys. Procedia* **37**, 1504–1510 (2013).
43. Li, X. et al. Electron counting and beam-induced motion correction enable near-atomic-resolution single-particle cryo-EM. *Nat. Methods* **10**, 584–590 (2013).
44. Stevens, A., Yang, H., Carin, L., Arslan, I. & Browning, N. D. The potential for Bayesian compressive sensing to significantly reduce electron dose in high-resolution STEM images. *Microscopy* **63**, 41–51 (2014).
45. Masiel, D. J., Bloom, R. S., Park, S. T. & Reed, B. W. Temporal compressive sensing instrumentation for TEM. *Microsc. Microanal.* **25**, S20–S21 (2017).
46. Rose, A. Television pickup tubes and the problem of noise. *Adv. Electron.* **1**, 131–166 (1948).
47. Egerton, R. F. Control of radiation damage in the TEM. *Ultramicroscopy* **127**, 100–108 (2013).
48. Rez, P. Comparison of phase contrast transmission electron microscopy with optimized scanning transmission annular dark field imaging for protein imaging. *Ultramicroscopy* **96**, 117–124 (2003).
49. Joy, D. C. & Joy, C. S. Scanning electron microscope imaging in liquids — some data on electron interactions in water. *J. Microsc.* **221**, 84–99 (2005).
50. Colliex, C., Mory, C., Olins, A. L., Olins, D. E. & Tencé, D. E. Energy filtered STEM imaging of thick biological sections. *J. Microsc.* **153**, 1–21 (1989).
51. Park, J. et al. Direct observation of wet biological samples by graphene liquid cell transmission electron microscopy. *Nano Lett.* **15**, 4737–4744 (2015).
52. Liao, H.-G., Cui, L., Whitelam, S. & Zheng, H. Real-time imaging of Pt₃Fe nanorod growth in solution. *Science* **336**, 1011–1014 (2012).
53. Peckys, D. B., Veith, G. M., Joy, D. C. & de Jonge, N. Nanoscale imaging of whole cells using a liquid enclosure and a scanning transmission electron microscope. *PLOS ONE* **4**, e8214 (2009).
54. Klein, K. L., Anderson, I. M. & de Jonge, N. Transmission electron microscopy with a liquid flow cell. *J. Microsc.* **242**, 117–123 (2011).
55. Ring, E. A. & de Jonge, N. Video-frequency scanning transmission electron microscopy of moving gold nanoparticles in liquid. *Micron* **43**, 1078–1084 (2012).
56. Thust, A., Coene, W. M. J., Op de Beeck, M. & Van Dyck, D. Focal-series reconstruction in HRTEM: simulation studies on non-periodic objects. *Ultramicroscopy* **64**, 211–230 (1996).
57. Kisielowski, C. et al. Imaging columns of the light elements carbon, nitrogen and oxygen with sub angstrom resolution. *Ultramicroscopy* **89**, 243–263 (2001).
58. Haider, M. et al. A spherical-aberration-corrected 200 kV transmission electron microscope. *Ultramicroscopy* **75**, 53–60 (1998).
59. Lentzen, M. et al. High-resolution imaging with an aberration-corrected transmission electron microscope. *Ultramicroscopy* **92**, 233–242 (2002).
60. Coene, W. & Jansen, A. J. Image delocalisation and high resolution transmission electron microscopic imaging with a field emission gun. *Scan. Microsc.* **6**, S379–S403 (1992).
61. Cervera Gontard, L., Dunin-Borkowski, R. E., Hytch, M. J. & Ozkaya, D. Delocalisation in images of Pt nanoparticles. *J. Phys. Chem. Ser. B* **26**, 292–295 (2006).
62. Borisevich, A. Y., Lupini, A. R. & Pennycook, S. J. Depth sectioning with the aberration-corrected scanning transmission electron microscope. *Proc. Natl Acad. Sci. USA* **103**, 3044–3048 (2006).
63. de Jonge, N., Sougrat, R., Northan, B. M. & Pennycook, S. J. Three-dimensional scanning transmission electron microscopy of biological specimens. *Microsc. Microanal.* **16**, 54–63 (2010).
64. Nellist, P. D., Cosgriff, E. C., Behan, G. & Kirkland, A. I. Imaging modes for scanning confocal electron microscopy in a double aberration-corrected transmission electron microscope. *Microsc. Microanal.* **14**, 82–88 (2008).
65. Jia, C. L., Lentzen, M. & Urban, K. Atomic-resolution imaging of oxygen in perovskite ceramics. *Science* **299**, 870–873 (2003).
66. Jia, C. L. et al. Atomic-scale study of electric dipoles near charged and uncharged domain walls in ferroelectric films. *Nat. Mater.* **7**, 57–61 (2008).
67. Jia, C. L., Houben, L., Thust, A. & Barthel, J. On the benefit of the negative-spherical-aberration imaging technique for quantitative HRTEM. *Ultramicroscopy* **110**, 500–505 (2010).
68. Jia, C. L. et al. Atomic-scale measurement of structure and chemistry of a single-unit-cell layer of LaAlO₃ embedded in SrTiO₃. *Microsc. Microanal.* **19**, 310–318 (2013).
69. Takeda, S., Kuwauchi, Y. & Yoshida, H. Environmental transmission electron microscopy for catalyst materials using a spherical aberration corrector. *Ultramicroscopy* **151**, 178–190 (2015).
70. Hansen, T. W. & Wagner, J. B. Environmental transmission electron microscopy in an aberration-corrected environment. *Microsc. Microanal.* **18**, 684–690 (2012).
71. Barthel, J. & Thust, A. On the optical stability of high-resolution transmission electron microscopes. *Ultramicroscopy* **134**, 6–17 (2013).
72. Tromp, R. M. & Schramm, S. M. Optimization and stability of the contrast transfer function in aberration-corrected electron microscopy. *Ultramicroscopy* **125**, 72–80 (2013).
73. Haider, M., Hartel, P., Müller, H., Uhlemann, S. & Zach, J. Information transfer in a TEM corrected for spherical and chromatic aberration. *Microsc. Microanal.* **16**, 393–408 (2010).
74. Zach, J. Chromatic correction: a revolution in electron microscopy? *Phil. Trans. R. Soc. A* **367**, 3699–3707 (2009).
75. Rose, H. H. Future trends in aberration-corrected electron microscopy. *Phil. Trans. R. Soc. A* **367**, 3809–3823 (2009).
76. Kabius, B. et al. First application of C_c-corrected imaging for high-resolution and energy-filtered TEM. *J. Electron. Microsc.* **58**, 147–155 (2009).
77. Leary, R. & Brydson, R. Chromatic aberration correction: the next step in electron microscopy. *Adv. Imag. Electron. Phys.* **165**, 73–130 (2011).
78. Forbes, B. D., Houben, L., Mayer, J., Dunin-Borkowski, R. E. & Allen, L. J. Elemental mapping in achromatic atomic-resolution energy-filtered transmission electron microscopy. *Ultramicroscopy* **147**, 98–105 (2014).
79. Urban, K. W. et al. Achromatic elemental mapping beyond the nanoscale in the transmission electron microscope. *Phys. Rev. Lett.* **110**, 185507 (2013).
80. Reimer, L. & Ross-Messemer, M. Top-bottom effect in energy-selecting transmission electron microscopy. *Ultramicroscopy* **21**, 385–387 (1987).
81. Baudoin, J. P., Jinschek, J. R., Boothroyd, C. B., Dunin-Borkowski, R. E. & de Jonge, N. Chromatic aberration-corrected tilt series transmission electron microscopy of nanoparticles in a whole mount macrophage cell. *Microsc. Microanal.* **19**, 814–820 (2013).
82. Danev, R. & Nagayama, K. Transmission electron microscopy with Zernike phase plate. *Ultramicroscopy* **88**, 243–252 (2001).
83. Danev, R., Buijsse, B., Khoshouei, M., Plitzko, J. M. & Baumeister, W. Volta potential phase plate for in-focus phase contrast transmission electron microscopy. *Proc. Natl Acad. Sci. USA* **111**, 15635–15640 (2014).
84. Prozorov, T., Almeida, T. P., Kovacs, A. & Dunin-Borkowski, R. E. Off-axis electron holography of bacterial cells and magnetic nanoparticles in liquid. *J. R. Soc. Interface* **14**, 20170464 (2017).
85. Shirai, M. et al. In situ electron holographic study of ionic liquid. *Ultramicroscopy* **146**, 125–129 (2014).
86. Dunin-Borkowski, R. E. & Houben, L. in *Liquid Cell Electron Microscopy* (ed. Ross, F. M.) 408–433 (Cambridge Univ. Press, 2016).
87. Tanigaki, T. et al. Magnetic field observations in CoFeB/Ta layers with 0.67-nm resolution by electron holography. *Sci. Rep.* **7**, 16598 (2017).
88. Linck, M. et al. Chromatic aberration correction for atomic resolution TEM imaging from 20 to 80 kV. *Phys. Rev. Lett.* **117**, 076101 (2016).
89. Demers, H., Poirier-Demers, N., Drouin, D. & de Jonge, N. Simulating STEM imaging of nanoparticles in micrometers-thick substrates. *Microsc. Microanal.* **16**, 795–804 (2010).

90. Beszterjan, S. et al. Visualization of cellular components in a mammalian cell with liquid-cell transmission electron microscopy. *Microsc. Microanal.* **23**, 46–55 (2017).
91. de Jonge, N., Verch, A. & Demers, H. The influence of beam broadening on the spatial resolution of annular dark field scanning transmission electron microscopy. *Microsc. Microanal.* **24**, 8–16 (2018).
92. Zaluzec, N. J. The influence of C_2/C_c correction in analytical imaging and spectroscopy in scanning and transmission electron microscopy. *Ultramicroscopy* **151**, 240–249 (2015).
93. Hohmann-Marriott, M. F. et al. Nanoscale 3D cellular imaging by axial scanning transmission electron tomography. *Nat. Methods* **6**, 729–731 (2009).
94. Hyun, J. K., Ercius, P. & Muller, D. A. Beam spreading and spatial resolution in thick organic specimens. *Ultramicroscopy* **109**, 1–7 (2008).
95. Wolf, S. G., Houben, L. & Elbaum, M. Cryo-scanning transmission electron tomography of vitrified cells. *Nat. Methods* **11**, 423–428 (2014).
96. Lazić, I. & Bosch, E. G. T. Analytical review of direct STEM imaging techniques for thin samples. *Adv. Imag. Electron. Phys.* **199**, 75–184 (2018).
97. Jungjohann, K. L., Evans, J. E., Aguiar, J. A., Arslan, I. & Browning, N. D. Atomic-scale imaging and spectroscopy for in situ liquid scanning transmission electron microscopy. *Microsc. Microanal.* **18**, 621–627 (2012).
98. Unocic, R. R. et al. Direct-write liquid phase transformations with a scanning transmission electron microscope. *Nanoscale* **8**, 15581–15588 (2016).
99. Wang, C., Qiao, Q., Shokuhfar, T. & Klie, R. F. High-resolution electron microscopy and spectroscopy of ferritin in biocompatible graphene liquid cells and graphene sandwiches. *Adv. Mater.* **26**, 3410–3414 (2014).
100. Barth, J. E. & Kruij, P. Addition of different contributions to the charged particle probe size. *Optik* **101**, 101–109 (1996).
101. van Benthem, K. et al. Three-dimensional ADF imaging of individual atoms by through-focal series stem. *Ultramicroscopy* **106**, 1062–1068 (2006).
102. Dahmen, T., Trampert, P., de Jonge, N. & Slusallek, P. Advanced recording schemes for electron tomography. *MRS Bull.* **41**, 537–541 (2016).
103. Einstein, A. On the motion — required by the molecular kinetic theory of heat — of small particles suspended in a stationary liquid. *Ann. Phys.* **17**, 549–560 (1905).
104. Browning, N. D. & Evans, J. E. in *Liquid Cell Electron Microscopy* (ed. Ross, F. M.) 456–475 (Cambridge Univ. Press, 2016).
105. Chee, S. W., Baraissov, Z., Loh, N. D., Matsudaira, P. T. & Mirsaidov, U. Desorption-mediated motion of nanoparticles at the liquid-solid interface. *J. Phys. Chem. C* **120**, 20462–20470 (2016).
106. Chee, S. W., Loh, D., Mirsaidov, U. & Matsudaira, P. Probing nanoparticle dynamics in 200 nm thick liquid layers at millisecond time resolution. *Microsc. Microanal.* **21** (Suppl. 3), 267–268 (2015).
107. Tian, X., Zheng, H. & Mirsaidov, U. Aggregation dynamics of nanoparticles at solid-liquid interfaces. *Nanoscale* **9**, 10044–10050 (2017).
108. Chen, X. & Wen, J. In situ wet-cell TEM observation of gold nanoparticle motion in an aqueous solution. *Nanoscale Res. Lett.* **7**, 598 (2012).
109. White, E. R., Mecklenburg, M., Shevitski, B., Singer, S. B. & Regan, B. C. Charged nanoparticle dynamics in water induced by scanning transmission electron microscopy. *Langmuir* **28**, 3695–3698 (2012).
110. Liu, Y., Lin, X.-M., Sun, Y. & Rajh, T. In situ visualization of self-assembly of charged gold nanoparticles. *J. Am. Chem. Soc.* **135**, 3764–3767 (2013).
111. Tan, S. F., Chee, S. W., Lin, G. H. & Mirsaidov, U. Direct observation of interactions between nanoparticles and nanoparticle self-assembly in solution. *Acc. Chem. Res.* **50**, 1303–1312 (2017).
112. Verch, A., Pfaff, M. & De Jonge, N. Exceptionally slow movement of gold nanoparticles at a solid:liquid interface investigated by scanning transmission electron microscopy. *Langmuir* **31**, 6956–6964 (2015).
113. Jiang, N. Note on in situ (scanning) transmission electron microscopy study of liquid samples. *Ultramicroscopy* **179**, 81–83 (2017).
114. Parent, L. R. et al. Tackling the challenges of dynamic experiments using liquid-cell transmission electron microscopy. *Acc. Chem. Res.* **51**, 3–11 (2018).
115. LaGrange, T. et al. Nanosecond time-resolved investigations using the in situ of dynamic transmission electron microscope (DTEM). *Ultramicroscopy* **108**, 1441–1449 (2008).
116. Fu, X., Chen, B., Tang, J., Hassan, M. T. & Zewail, A. H. Imaging rotational dynamics of nanoparticles in liquid by 4D electron microscopy. *Science* **355**, 494–498 (2017).
117. Evans, J. E., Jungjohann, K. L., Browning, N. D. & Arslan, I. Controlled growth of nanoparticles from solution with in situ liquid transmission electron microscopy. *Nano Lett.* **11**, 2809–2813 (2011).
118. Alloeyeau, D. et al. Unravelling kinetic and thermodynamic effects on the growth of gold nanoplates by liquid transmission electron microscopy. *Nano Lett.* **15**, 2574–2581 (2015).
119. Grogan, J. M., Schneider, N. M., Ross, F. M. & Bau, H. H. Bubble and pattern formation in liquid induced by an electron beam. *Nano Lett.* **14**, 359–364 (2014).
120. White, E. R. et al. In situ transmission electron microscopy of lead dendrites and lead ions in aqueous solution. *ACS Nano* **6**, 6308–6317 (2012).
121. Sang, X. H. et al. Dynamic scan control in STEM: spiral scans. *Adv. Struct. Chem. Imaging* **2**, 6 (2016).
122. De Yoreo, J. J. & Sommerdijk, N. A. J. M. Investigating materials formation with liquid-phase and cryogenic TEM. *Nat. Rev. Mater.* **1**, 16035 (2016).
123. Park, J. H. et al. Control of electron beam-induced Au nanocrystal growth kinetics through solution chemistry. *Nano Lett.* **15**, 5314–5320 (2015).
124. de Jonge, N., Browning, N., Evans, J. E., Chee, S. W. & Ross, F. M. in *Liquid Cell Electron Microscopy* (ed. Ross, F. M.) 164–188 (Cambridge Univ. Press, 2016).
125. Freitag, B., Kujawa, S., Mul, P. M., Ringnald, J. & Tiemeijer, P. C. Breaking the spherical and chromatic aberration barrier in transmission electron microscopy. *Ultramicroscopy* **102**, 209–214 (2005).
126. Krivanek, O. L., Kundmann, M. K. & Kimoto, K. Spatial resolution in EFTEM elemental maps. *J. Microsc.* **180**, 277–287 (1995).

Acknowledgements

N.d.J. acknowledges H. Demers, T. Dahmen, M. Elbaum, D. Peckys and S. Wolf for discussions, a fellowship of the Visiting Faculty Program of the Weizmann Institute and E. Arzt for his support through the Leibniz Institute for New Materials (INM). L.H. and R.E.D.-B. are grateful to M. Luysberg, J. Barthel, A. Thust, K. Urban, S. Mi, C. Boothroyd, A. Kovács, J. Mayer, L. Allen, B. Forbes, J. Jinschek, J.-P. Baudoin, L. Cervera Gontard, D. Ozkaya, T. Hansen and M. Bar Sadan for discussions. F.M.R. acknowledges J.H. Park, N. Browning, S.W. Chee, J. Evans, D. Muller, R. Tromp and J. Hannon for helpful discussions.

Author contributions

All authors contributed to the discussion of content and researched data for the article. R.E.D.-B. and L.H. wrote the section on aberration correction. N.d.J. and F.M.R. wrote the sections on spatial and temporal resolution. All authors edited the article prior to submission.

Competing interests

The authors declare no competing interests.

Publisher's note

Springer Nature remains neutral with regard to jurisdictional claims in published maps and institutional affiliations.

Supplementary information

Supplementary information is available for this paper at <https://doi.org/10.1038/s41578-018-0071-2>.